64-11

PHILCO
A SUBSIDIARY OF Ford Motor Company
RESEARCH LABORATORIES

PHILCO
A SUBSIDIARY OF Ford Motor Company
RESEARCH LABORATORIES

Secondary Publication No. U-2543

RPL-TDR-64-45

THIRD QUARTERLY TECHNICAL REPORT

INTERNAL ENVIRONMENT OF SOLID ROCKET NOZZLES

Reporting Period: 1 December 1963 to 29 February 1964

Prepared for: Rocket Research Laboratories
Air Force Systems Command
Edwards, California

Under Contract: AF 04(611)-9072

Prepared by: F. C. Price, Project Manager
V. A. Marple
R. A. Dupuis

30 March 1964

ABSTRACT (U)

The Philco Reserach Laboratories are conducting a study of solid propellant nozzle environment to implement nozzle design methods. Study of the condensed phase effects is emphasized. Cold flow modeling technique has been developed to the point of showing quantitative particle impingement rates for the sixty-inch diameter engine modeled. Engine firing tests have provided the first data on heat fluxes to a molybdenum nozzle wall showing the effects of impinging alumina. A scanning spectrometer system has been completed for use in analyzing the alumina cloud emissivity. This is especially important in radiation calculations for large engines.

CONTENTS

ILLUSTRATIONS

ILLUSTRATIONS (Continued)

ILLUSTRATIONS (Continued)

ILLUSTRATIONS (Continued)

SECTION 1

INTRODUCTION

This project has the objective of studying the most enigmatic aspects of solid rocket nozzle environment - the condensed phase. Hot firings are being conducted with measurements of the radiation characteristics of the alumina cloud and determinations of heat flux effects on a nozzle caused by impinging alumina. Cold flow modeling is used to define the particle impingement and nozzle wall static pressure contours for various engine designs. The results of the work are to be applied to the practical problem of predicting these environmental factors in new engine designs.

A unique approach is taken in the test firings. Using the Philco Reserach Laboratories Simulator technique, data are obtained for heat flux both with and without alumina present, but at theoretically identical conditions of gas composition, pressure, velocity and temperature. Heat flux from particle impingement is computed from the molybdenum nozzle inner and outer transient surface temperatures during the several seconds of the firing. Heat flux from particle cloud radiation is taken within the chamber and at the throat using both a total radiation pyrometer and data from spectrometrically scanning the detailed cloud radiation. Tests are conducted with alumina solids added to a burning hydrogen-oxygen

system and with aluminum burned in the chamber in the presence of carbon-hydrogen-methanol-oxygen combustion.

The cold flow modeling approach uses scale models flowed under simularity conditions with nitrogen or with sulfur hexafluoride for a better heat capacity ratio simulation. Particles are injected and their impingement is determined by counting impinged particles on sticky tapes placed along the internal contours of the model nozzle. An ejector is to be used to produce subatmospheric pressures for exit cone studies. The particles are uniform polystyrene spheres of sizes 0.8 to 3.0 microns. Such particles are needed to fulfill the modeling simularity requirements.

Up to the middle of the third quarter of the program the work was largely concentrated on the facility and technique development for testing. It cannot be overemphasized that the development of meaningful data from modeling or firing using micron-sized particles requires a most rigorous approach in experimental technique.

This report shows the first data having practical significance both in modeling and test firing. The most meaningful testing phase of the program is occuring during the tenth month of the contract. The rapid scan spectrometer for particle cloud radiation analysis has been put into operation. The details of its installation and the first results are given.

Spectra have been produced illustrating the differences found between "clean" gas and particle clouds in radiation details. The actual heat flux due to particle impingement is presented for several of the first tests.

Particle impingement data in modeling is presented in considerable detail showing (1) how data for various grain burn times correlate (2) an indication of the precision of the data and (3) the indicated particle impingement for a full scale engine computed from a series of runs.

SECTION 2

COLD-FLOW MODELING

The work in cold-flow modeling was comprised of considerable technique development. However, definitive results were obtained and are reported below.

The work of the quarter started with a number of changes in the facility to achieve better uniformity of particle distribution across the grain port. The subsonic region of the model of a gimballed nozzle for a 60-inch engine was then completely analysed for particle impingement. Three particle sizes and three burn-time instants were run on the model.

During the fourth quarter of the program the exit cone in a 5° canted position will also be studied.

2.1 FACILITY DESCRIPTION

The cold-flow modeling facility consists of the following:

a. Particle Injection System
b. Spray Mixing and Evaporation Chamber
c. Metering Orifice Section and Test Chamber
d. Pressure Reading System
e. Air Ejector
f. Test Items (nozzle and grain models)

a. Particle Injection System

This system consists of two sets of pneumatic atomizing spray nozzles; one set of six on each side of the spray mixing chamber (Fig. 1). For each run the particle-alcohol mixture is divided equally between the two particle tanks. After main chamber flow is established, valves at the bottom of the tanks are opened and the mixture is atomized into the spray mixing chamber.

b. Spray Mixing and Evaporation Chamber

The spray mixing chamber (Fig. 1) allows the atomized alcohol (with particles) to be mixed and evaporated into the main gas flow. The primary gas is introduced at three places; one at each set of atomizers and one in the center as shown in Fig. 1 . Either air, nitrogen, or sulfur hexafluoride can be used as the primary gas.

c. Metering Orifice Section and Test Chamber

From the spray mixing chamber the gas flows through a flow metering orifice and into the test chamber which holds the model. Fig. 2 shows the test chamber with a nozzle model in place.

d. Pressure Reading System

The pre-pressurizing system for the nozzle static pressures is also shown in Fig. 2 . Pre-pressurizing of the manometer tubes (Fig. 3) requires the use of an auxiliary pressure supply, three-way solenoid valves, and bleed valves. Each manometer is pre-pressurized by the auxiliary pressure supply to approximately the height of liquid (water or mercury) which will read out for the test. During the run, the three-way solenoid valves are switched to read the nozzle pressure contour.

e. Air Ejector

Fig. 4 shows the air ejector with diffuser used to achieve sub-atmospheric pressures during tests of particle impingement on the exit cone of the nozzle model.

f. Test Items

Three of the nozzle models are shown in Fig. 5 & 6. Fig. 5 is a full scale model of the simulator hardware used in hot firing studies of particle impingement. The diffuser adapter and gasket is attached. A soft rubber gasket makes a seal between the nozzle and the diffuser. Fig. 6

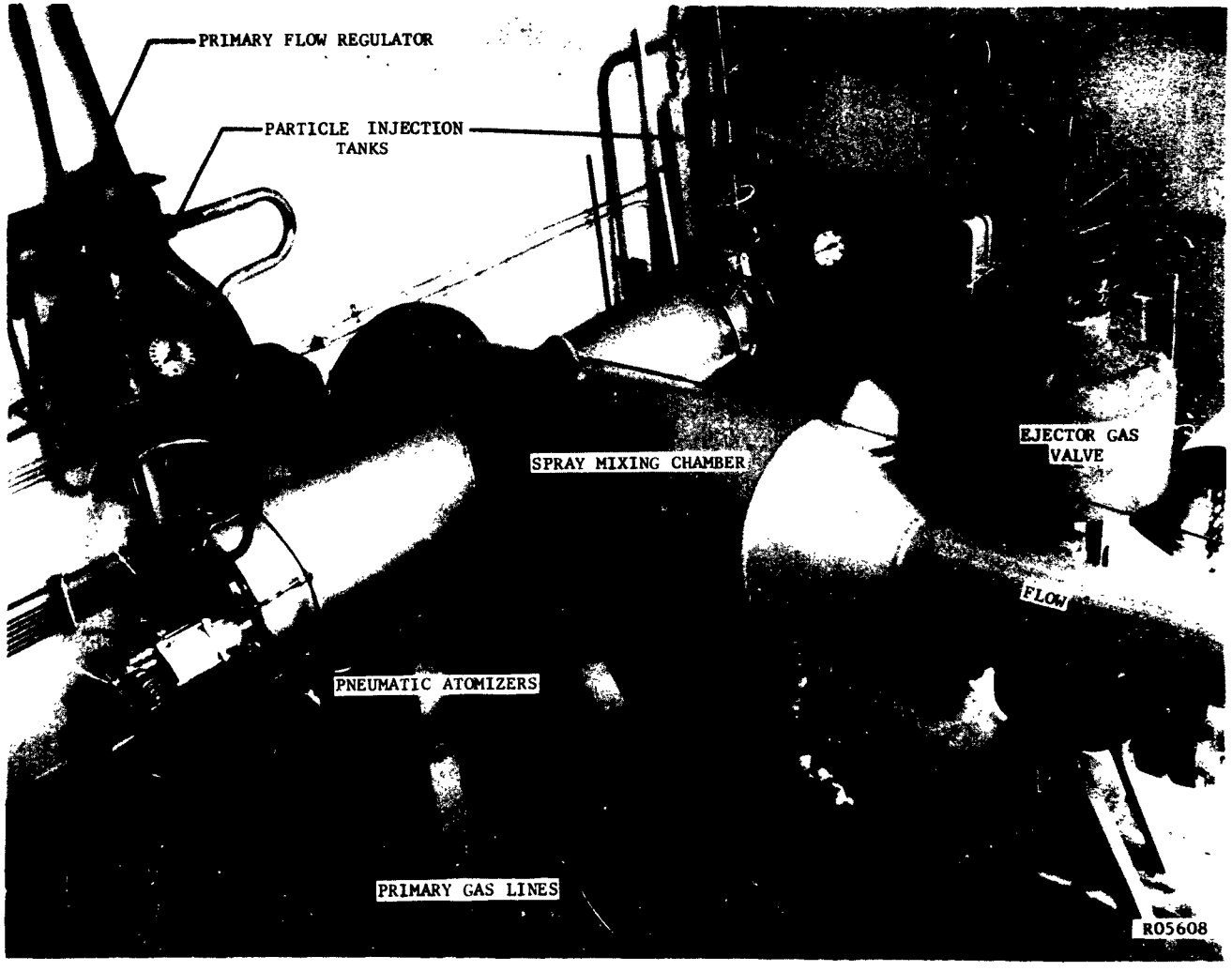

FIGURE 1. SPRAY MIXING CHAMBER WITH PARTICLE INJECTION SYSTEM

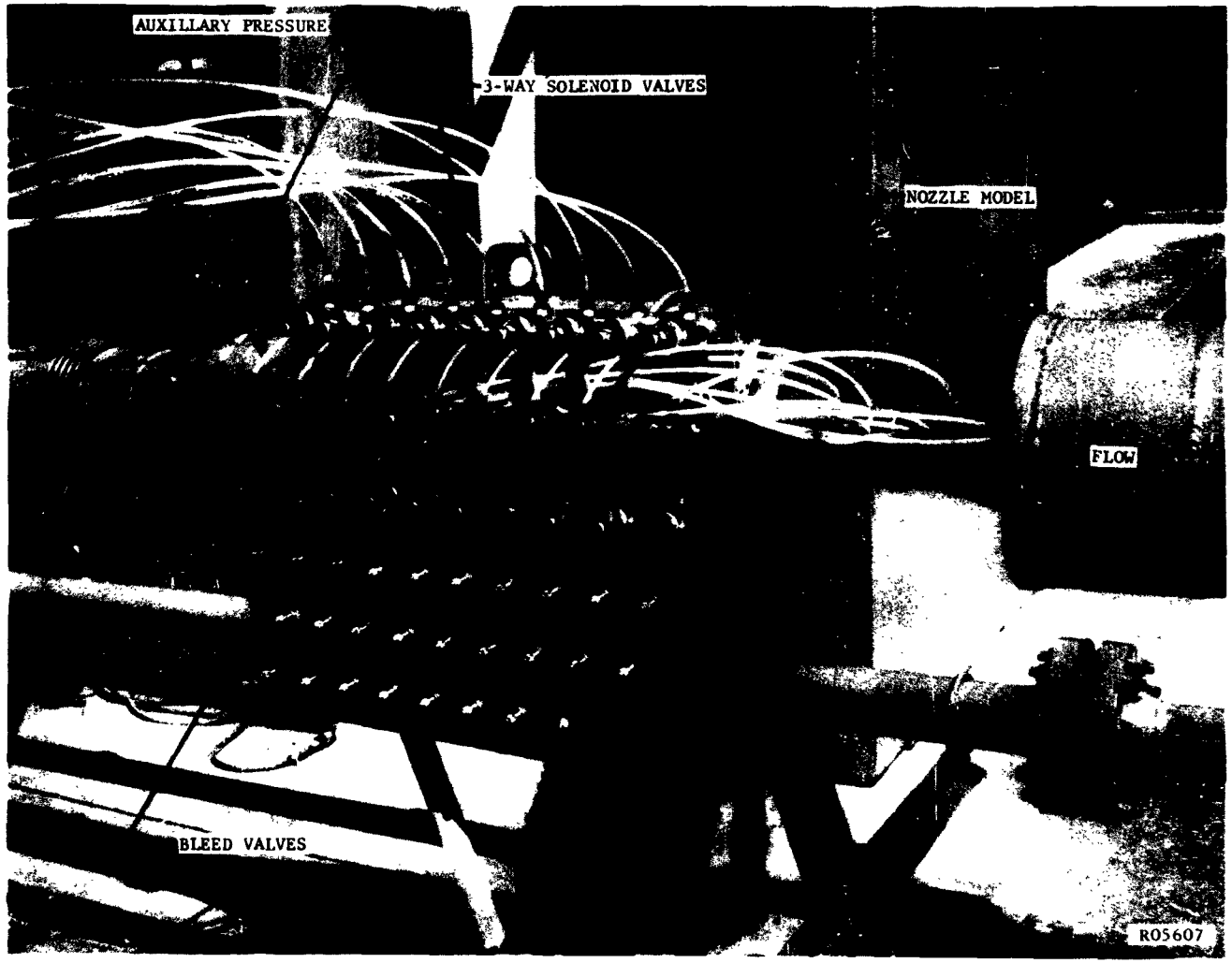

FIGURE 2. TEST CHAMBER WITH NOZZLE AND MANOMETER PRE-PRESSURIZING SYSTEM

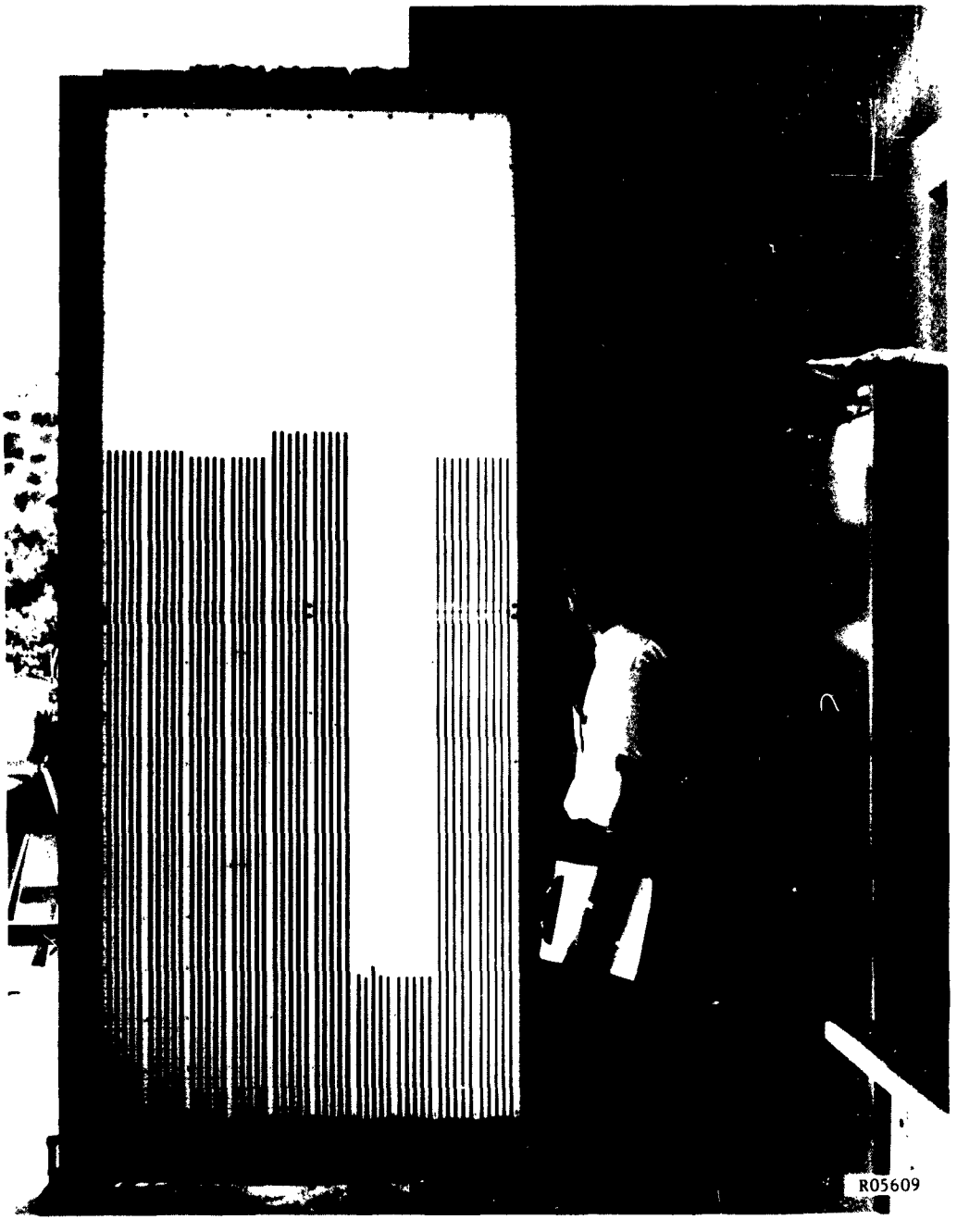

FIGURE 3. MANOMETER BOARD

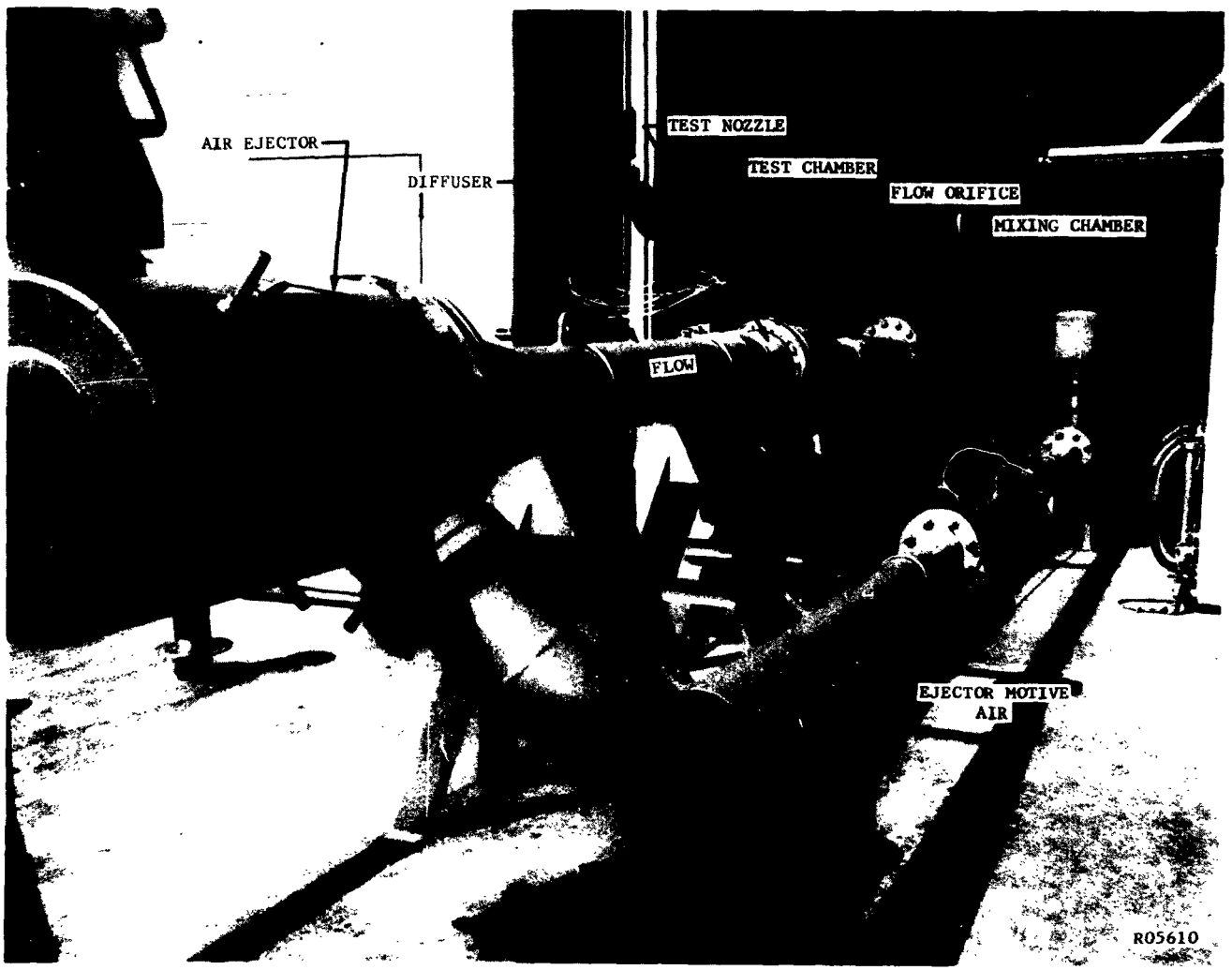

FIGURE 4. MODELING FACILITY

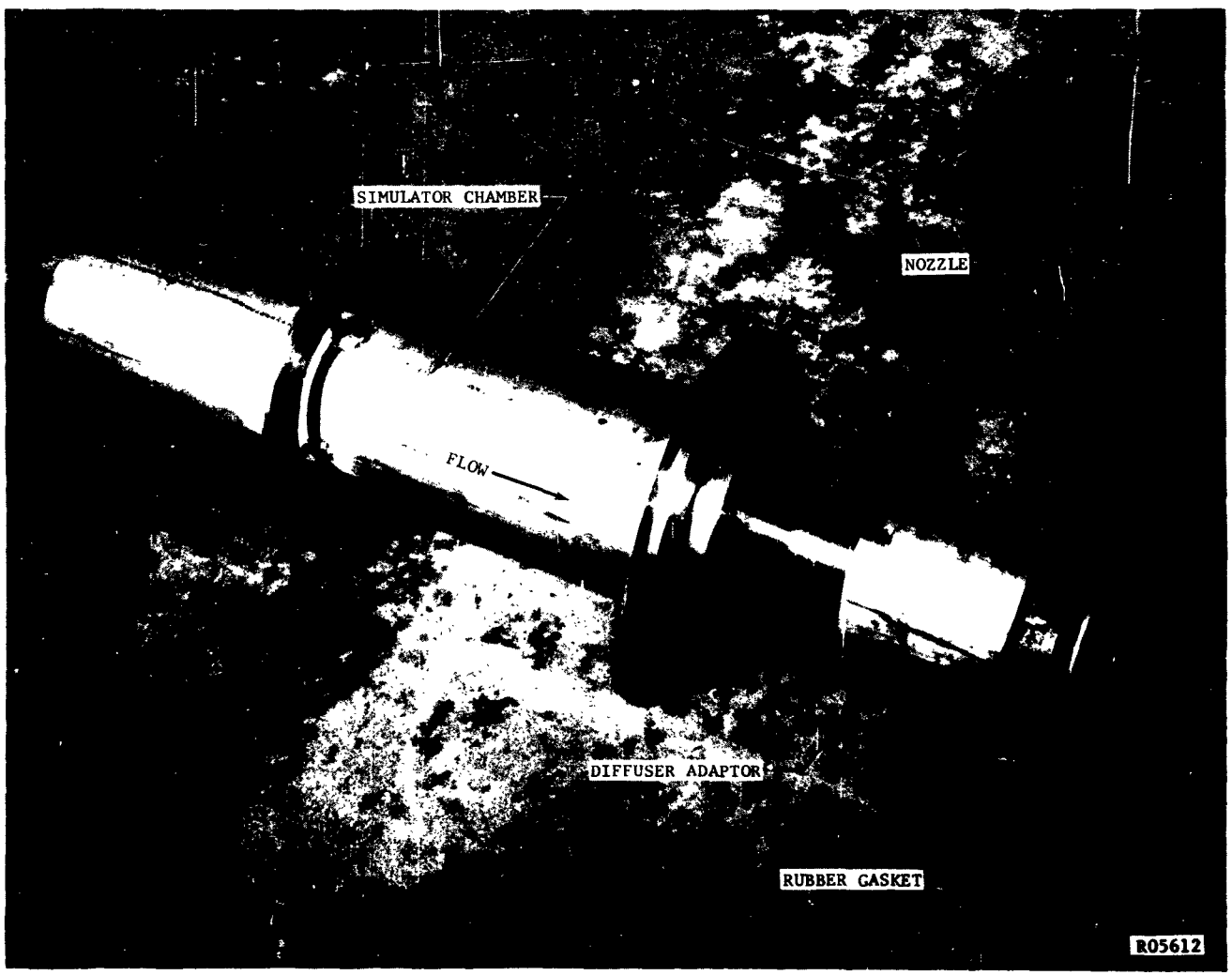

FIGURE 5. SIMULATOR MODEL

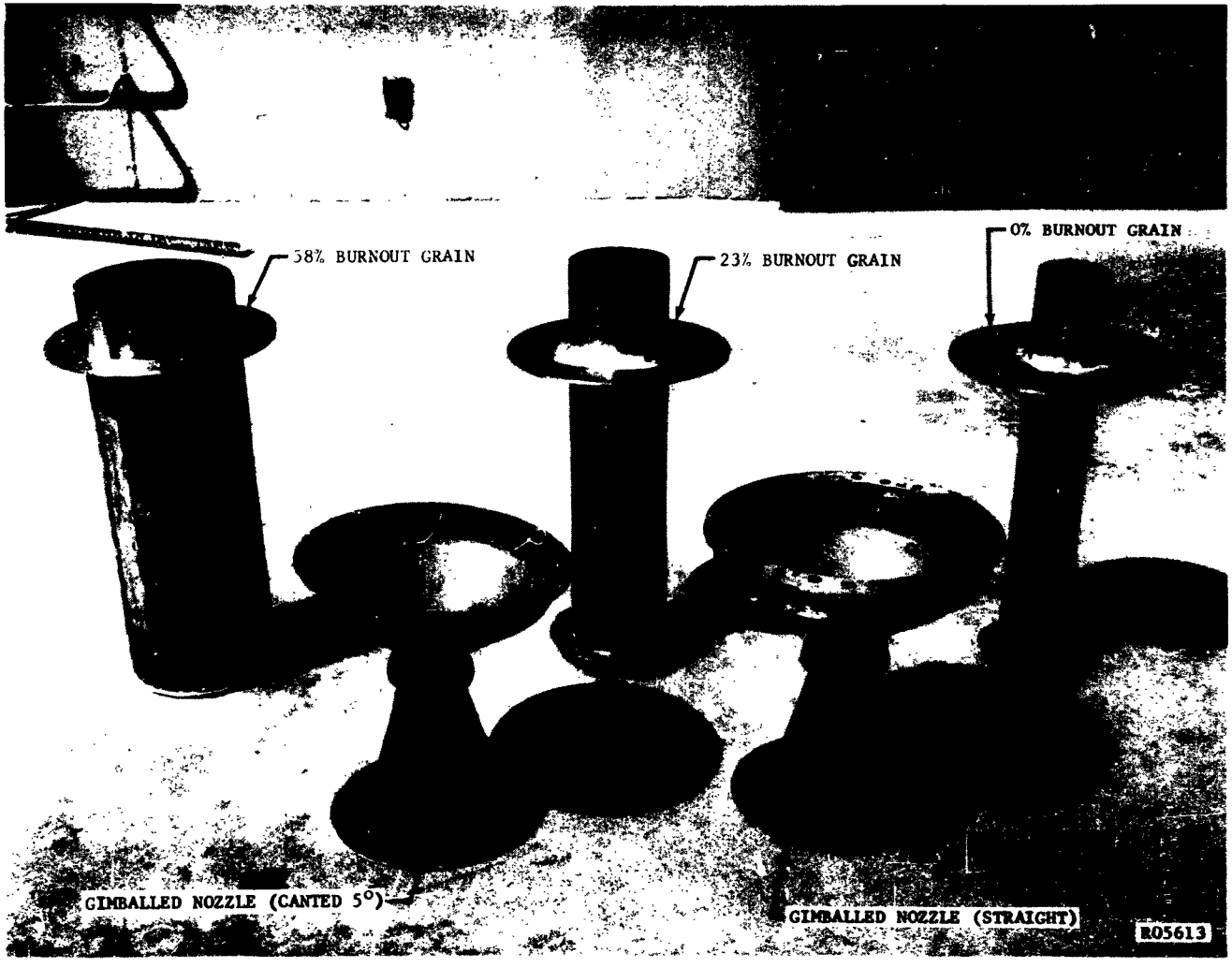

FIGURE 6. GIMBALLED NOZZLES AND GRAIN MODELS

shows the gimballed nozzle model in the straight and canted 5° positions. Also shown are three grain models corresponding to three different burn times.

For every run, particle receptor tapes are placed on bars inside the grain port to provide a record of the particle concentration distribution across the grain port, Fig. 7 . The long bar is vertical and the short one is horizontal. The tapes used to record the particle impingement along the nozzle wall (Fig. 8) are placed along the wall and then the grain model, with bars and tapes already installed, is clamped onto the nozzle. Fig. 8 shows a grain being put into the nozzle entrance. The large rubber seal at the end of the grain insures that there is no leak at the grain and nozzle interface. After each run, the tapes are removed and the particles counted under a microscope.

2.2 PARTICLE CONCENTRATION DISTRIBUTION ACROSS THE GRAIN PORT

The particles which impinge on the aft closure will have slipped from the gas streamlines only a very short distance. Therefore, in the model, the particle concentration distribution close to the grain port wall must be known and it should preferably be uniform across the model grain port.

One of the first grains tested was made from perforated metal. The perforated grain wall was intended to simulate more closely the flow from the burning grain and to prevent particle concentration along the wall. However, as was explained in the second quarterly[1], high wall concentrations were found in the perforated grain.

Three changes were then made in the test facility to correct this situation and a much better particle concentration distribution was obtained. It should be noted that after these changes were made, the perforated grain wall gave no better particle concentration distribution than a solid wall. Therefore all grain port models used are solid tubes as shown in Fig. 6. The three system changes were designed to improve the mixing of the gas and the atomized particle-alcohol mixture in the spray mixing chamber and to add a final mixing step downstream for the air and particles just before the flow enters the grain port.

The particle concentration distribution across the grain was determined by placing bars (with particle pick-up tapes) across the port and on the wall as shown in Fig. 7 . Fig. 9 shows the particle concentration distribution for the grain port shown in Fig. 7 .

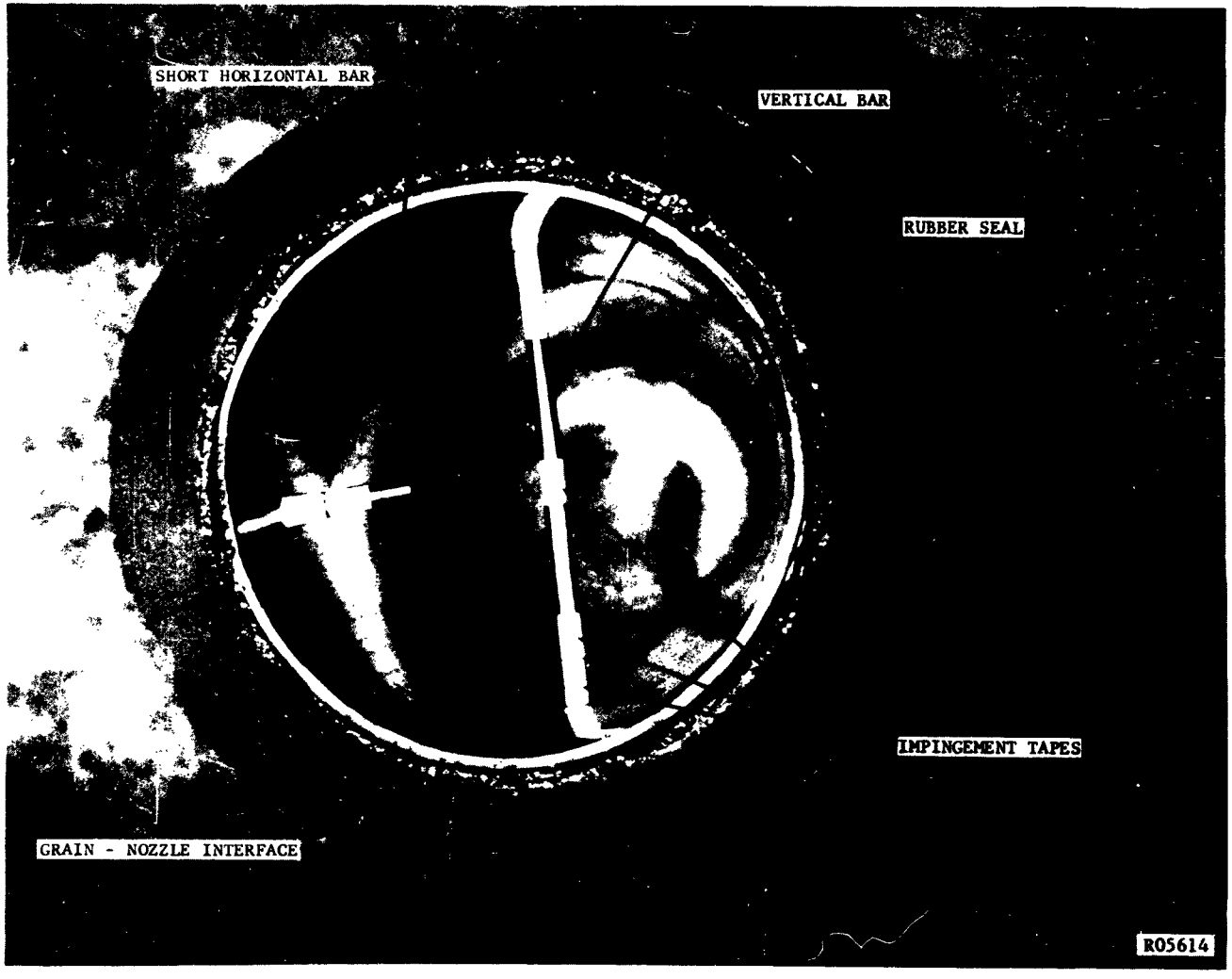

FIGURE 7. GRAIN PORT MODEL (LOOKING UPSTREAM FROM NOZZLE)

FIGURE 8. ASSEMBLY OF GRAIN PORT AND NOZZLE MODEL (WITH TAPES)

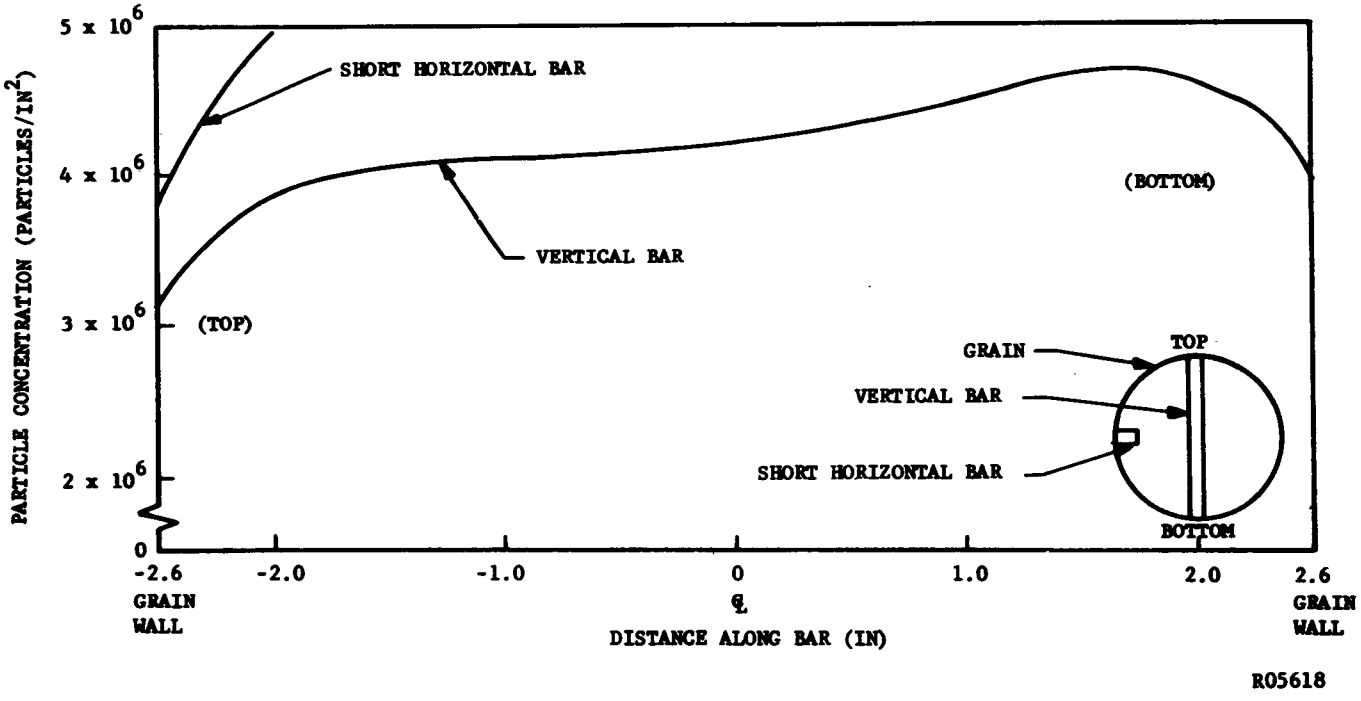

FIGURE 9. TYPICAL PARTICLE CONCENTRATION DISTRIBUTION IN GRAIN

By knowing (1) the particle concentration distribution across the grain port, (2) the particle concentration upstream of a tape on the aft closure, and (3) the total number of particles in the flow, the impingement data can be adjusted to account for what little unevenness there is in the particle concentration distribution.

2.3 DETERMINATION OF THE PARTICLE IMPINGEMENT IN A GIMBALLED NOZZLE

To demonstrate how particle impingement along the nozzle wall can be obtained from modeling, the gimballed nozzle has been chosen as an example. Since the ejector was not yet in operation the particle impingement was studied upstream of the throat. For the gimballed nozzle in straight position, this is where the major damage due to particle impingement is expected.

The modeling equations developed in the first quarterly[2] are restated here:

$$\frac{D_{P_M}}{D_{P_R}} = \frac{D_M}{D_R} \cdot \frac{\rho_{P_R}}{\rho_{P_M}} \cdot \frac{A_R}{A_M} \cdot \frac{\mu_M}{\mu_R}^{1/2}$$

$$P_M = \frac{D_{P_R}}{D_{P_M}} \frac{\mu_M}{\mu_R} \left[\frac{T_M}{T_R} \cdot \frac{MW_R}{MW_M} \cdot \frac{\gamma_R}{\gamma_M} \right]^{1/2} P_R$$

Where:

D_{P_M} = particle diameter in the model

D_{P_R} = hot particle diameter in the rocket

P_M = chamber pressure of the model

$\frac{D_R}{D_M}$ = scale factor = 5.75

ρ_{P_R} = rocket particle density = 2.28 gm/cm^3

ρ_{P_M} = model particle density = 1.05 gm/cm^3

Modeling gas is nitrogen.

A_M = sonic velocity at throat of model = 992 fps

A_R = sonic velocity at throat of rocket = 4100 fps

μ_M = viscosity of N_2 in model = 1.06×10^{-5} lb/ft sec.

μ_R = viscosity of gas in rocket = 6.7×10^{-5} lb/ft sec.

T_M = chamber temperature of N_2 in model = 477°R

T_R = chamber temperature of gas in rocket = 6360°R

MW_R = molecular weight of rocket exhaust = 20.4

MW_M = molecular weight of N_2 = 28

γ_R = specific heat of rocket exhaust = 1.18

γ_M = specific heat of N_2 = 1.4

Therefore, from the modeling equations, the particle diameter ratio and the model chamber pressure are:

$$\frac{D_{P_M}}{D_{P_R}} = \left[\frac{1}{5.75} \times \frac{2.28}{1.05} \times \frac{4100}{992} \times \frac{1.06 \times 10^{-5}}{6.7 \times 10^{-5}}\right]^{-1/2} = 0.496$$

and

$$P_M = \frac{1}{.496} \times \frac{1.06 \times 10^{-5}}{6.7 \times 10^{-5}} \times \left[\frac{477}{6360} \times \frac{20.4}{28} \times \frac{1.18}{1.4}\right]^{-1/2} \times 613 \text{ psia}$$

$$= 42 \text{ psia.}$$

Three sizes of polystyrene particles were used. Table I shows the sizes of aluminum oxide particles being modeled.

TABLE I

MODELED PARTICLE SIZE

Polystyrene Particle Dia.	Aluminum Oxide Particle Dia. in Rocket, Hot	Cold Aluminum Oxide Particle from Rocket
.8 μ	1.6 μ	1.4 μ
1.3 μ	2.6 μ	2.2 μ
2.05 μ	4.1 μ	3.5 μ

As shown in Fig. 10, three grain port sizes representing three different instants in burn-time were needed to show the variation of impingement with time. Since three grains and three particle sizes were used, a total of nine runs was needed to get the overall impingement picture. Photos of the nozzle model and the three grains are shown in Fig. 6.

Fig. 11, 12, and 13, present the impingement data of the 1.4 μ, 2.2 μ, and 3.5 μ particles, respectively. The ordinate is expressed as the weight percent of that particular particle size, at that particular instant of time, impinging on the aft closure. Each data point represents the average of from 6 to 12 counts of impinged particle density in the region of the particular position along the aft closure.

An axample is given to illustrate how the particles which are impinged on the tape of the model can be converted to weight percent impinged on the aft closure of the rocket: Assume counting by use of a microscope gives N particles/sq. in. on the tape at some point along the aft closure. Also, it is known that 10^{10} particles were originally injected into the gas and the scale factor from the model to the rocket is 5.75. Then the weight percent impinged is:

$$\frac{N}{10^{10}} \times \frac{1}{(5.75)^2} \times 100.$$

It is also interesting to note just how reproducible the data are by comparing one persons particle count with another's and by comparing two tapes from the same run or from duplicate runs. These comparisons, shown in Fig. 14, indicate reproducibility of the data.

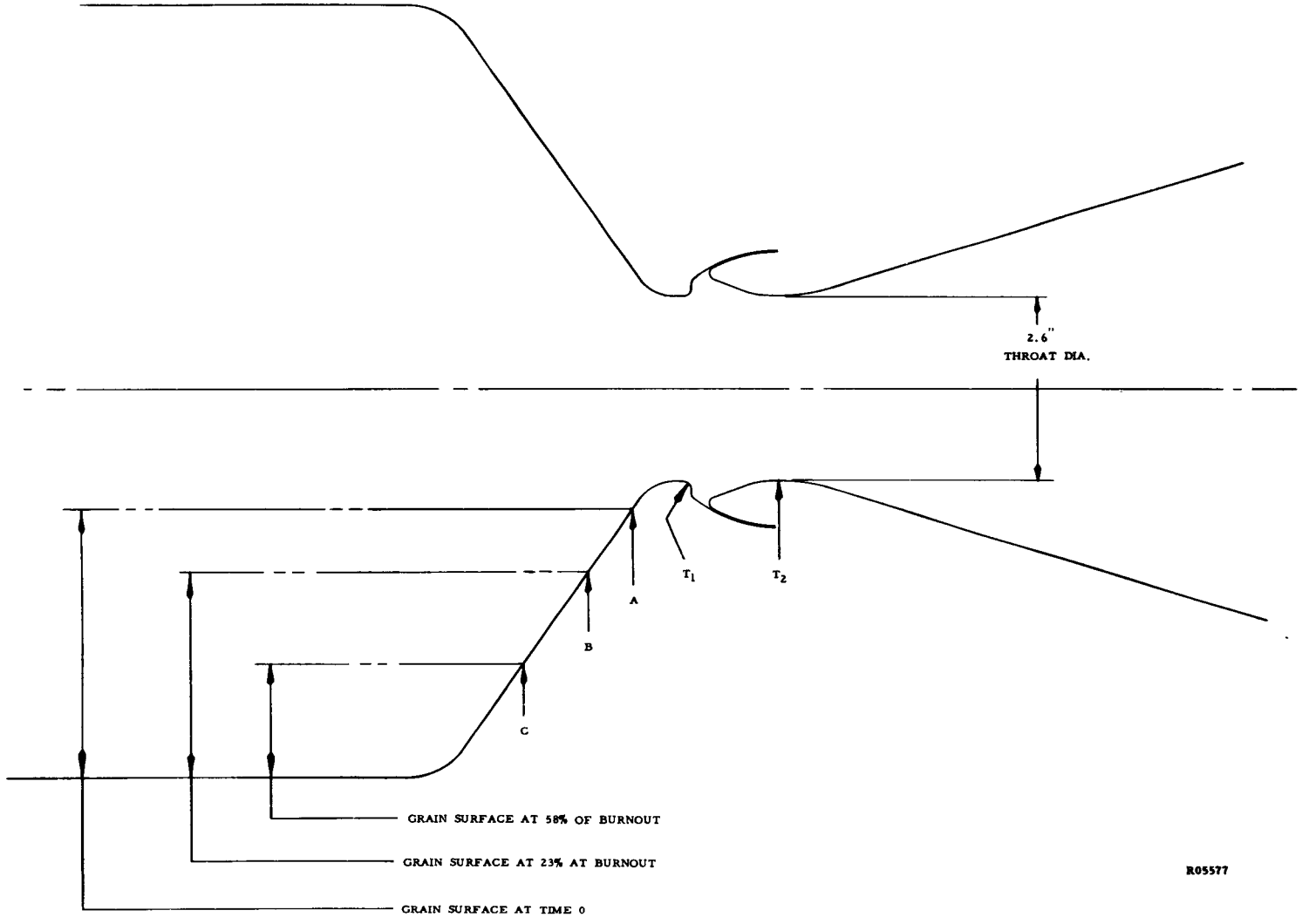

FIGURE 10. GIMBALLED NOZZLE AND GRAIN PORT CONFIGURATIONS

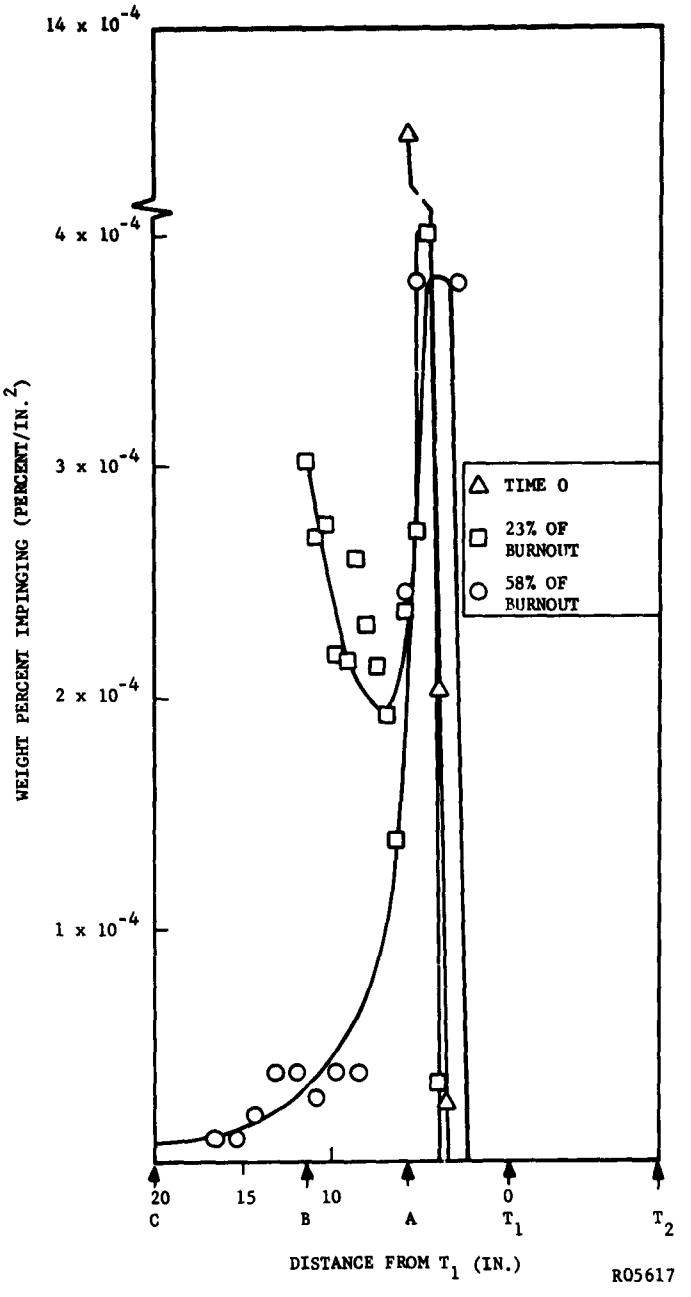

FIGURE 11. WEIGHT PERCENT OF 1.4μ PARTICLES IMPINGING ALONG THE AFT CLOSURE

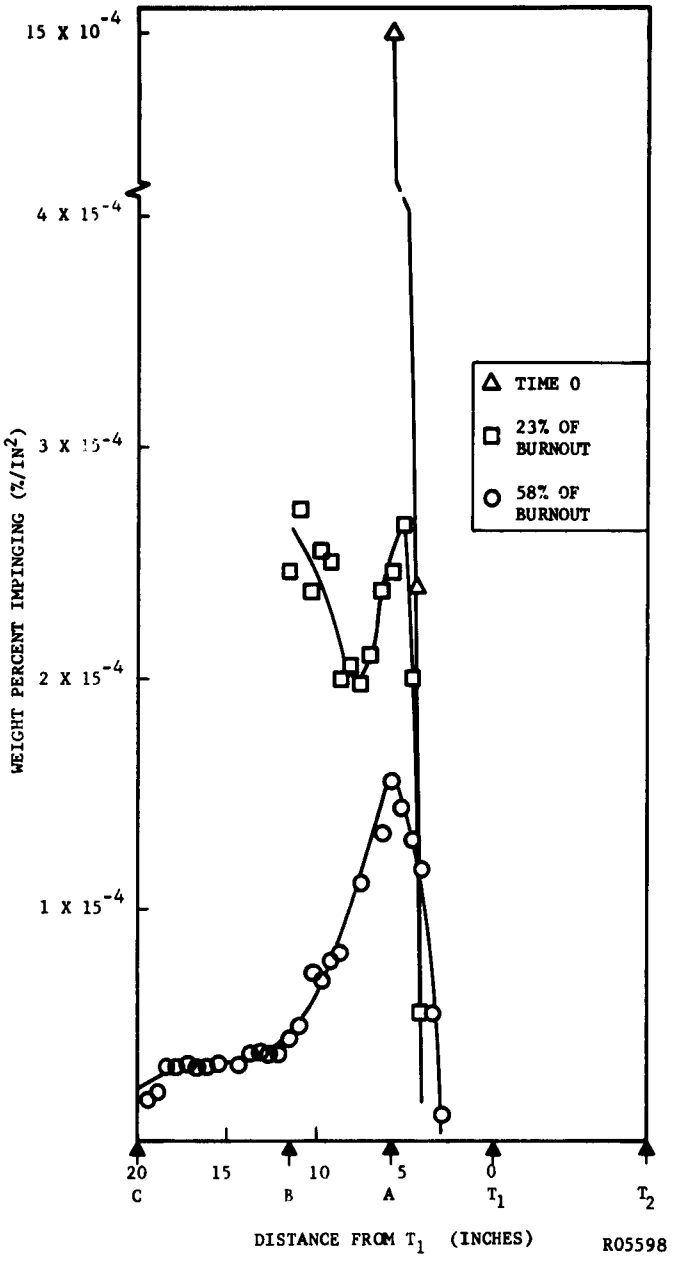

FIGURE 12. WEIGHT PERCENT OF 2.2μ PARTICLES IMPINGING ALONG THE AFT CLOSURE

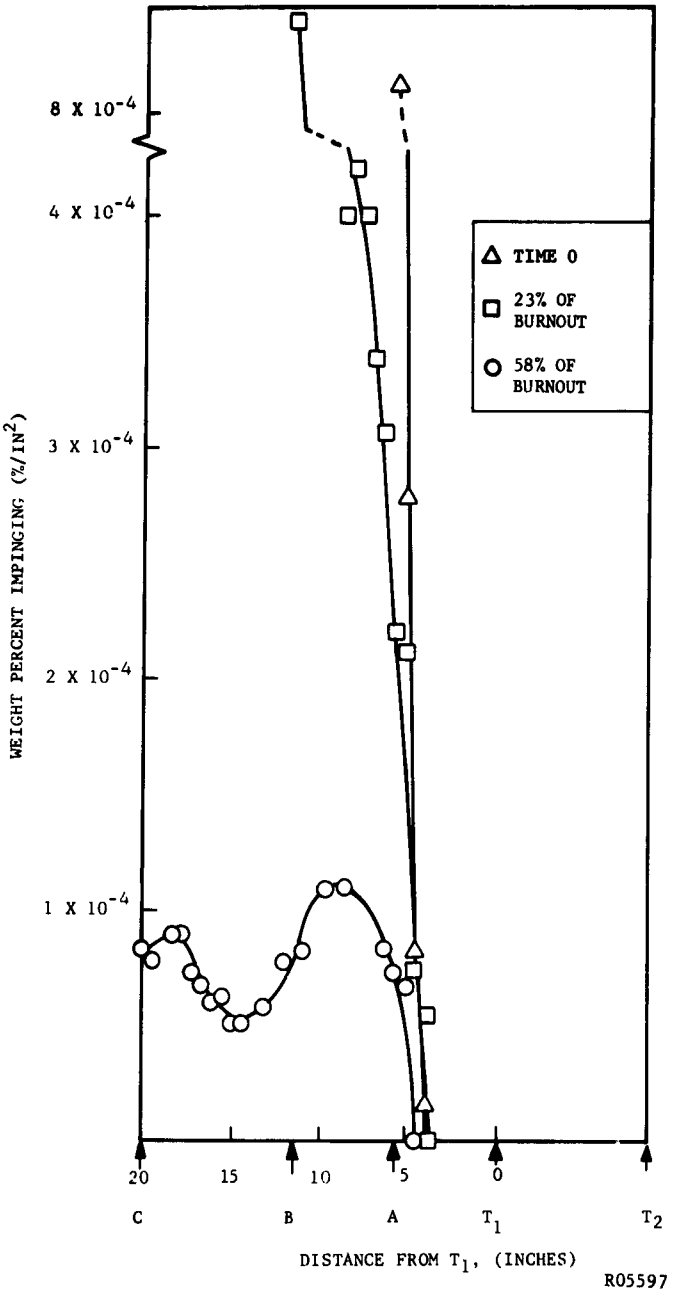

FIGURE 13. WEIGHT PERCENT OF 3.5μ PARTICLES IMPINGING ALONG THE AFT CLOSURE

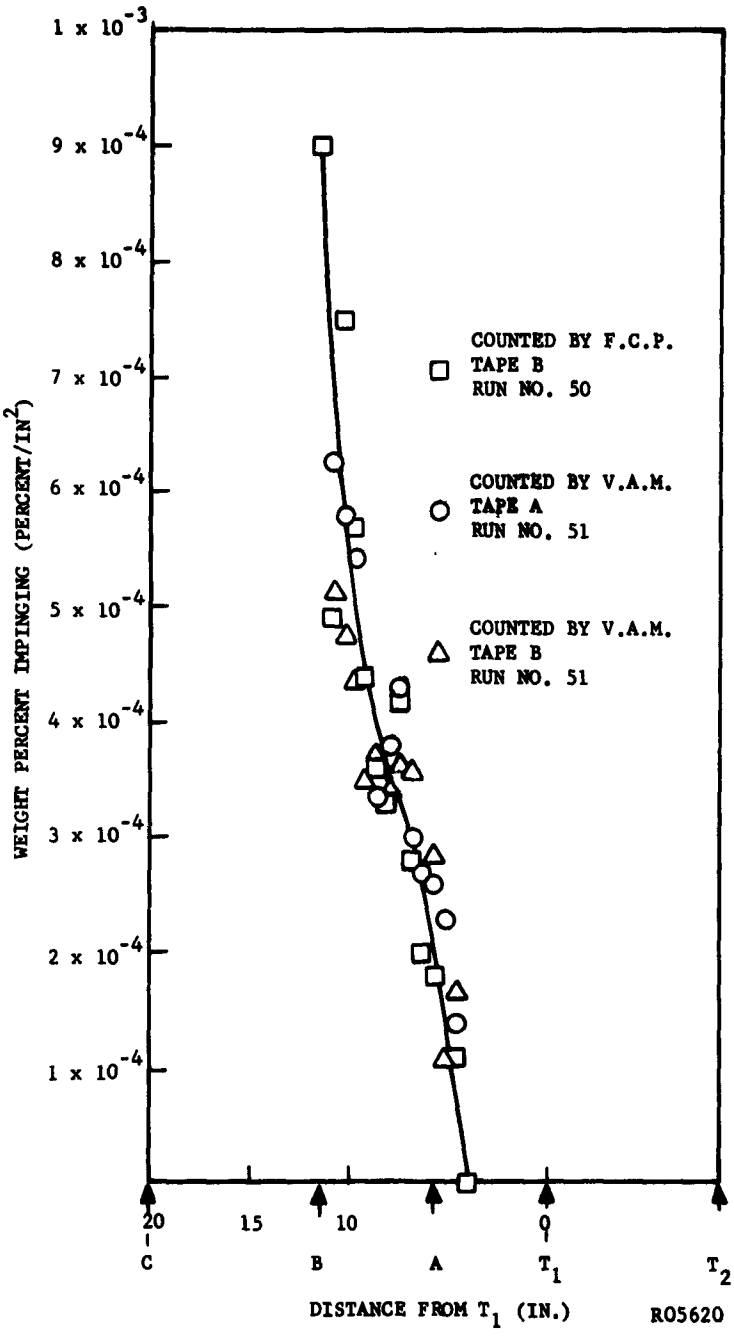

FIGURE 14. REPRODUCIBILITY OF IMPINGEMENT DATA

From Figures 11, 12, and 13 it is now possible to develop a curve of impingement versus grain burn-time for each particle size at any point along the aft closure. Fig. 15, 16, and 17 present such curves for points A, B, and C respectively. The ordinates of these curves have been changed to weight fraction impinging per sq. in. instead of weight percent impinging per sq. in. as in Fig. 11, 12, and 13.

From the curves in Fig. 15, 16, and 17, and average weight fraction impinged can be found from each particle size at points A, B, and C by noting:

$$\left(100-t_b\right) \frac{\delta w_i \{D\}}{\delta w \{D\}} = \int_{t_b}^{100} \frac{\delta w_i \{D\}}{\delta w \{D\}} \{t\}\, dt$$

Where: D is a particular particle size

$\frac{\delta w_i \{D\}}{\delta w \{D\}}$ = average weight fraction impinged per sq. in. for this particle size

$\frac{\delta w_i \{D\}}{\delta w \{D\}} \{t\}$ = weight fraction impinged per sq. in. for the same particle size as a function of time

t_b = time, percent of burnout when the point on the aft closure is first exposed to particle impingement

The integral $\int_{t_b}^{100} \frac{\delta w_i \{D\}}{\delta w \{D\}} \{t\}\, dt$ is the area under the curves of Figures 15, 16, and 17. Table II is a tabulation of $\frac{\delta w_i \{D\}}{\delta w \{D\}}$.

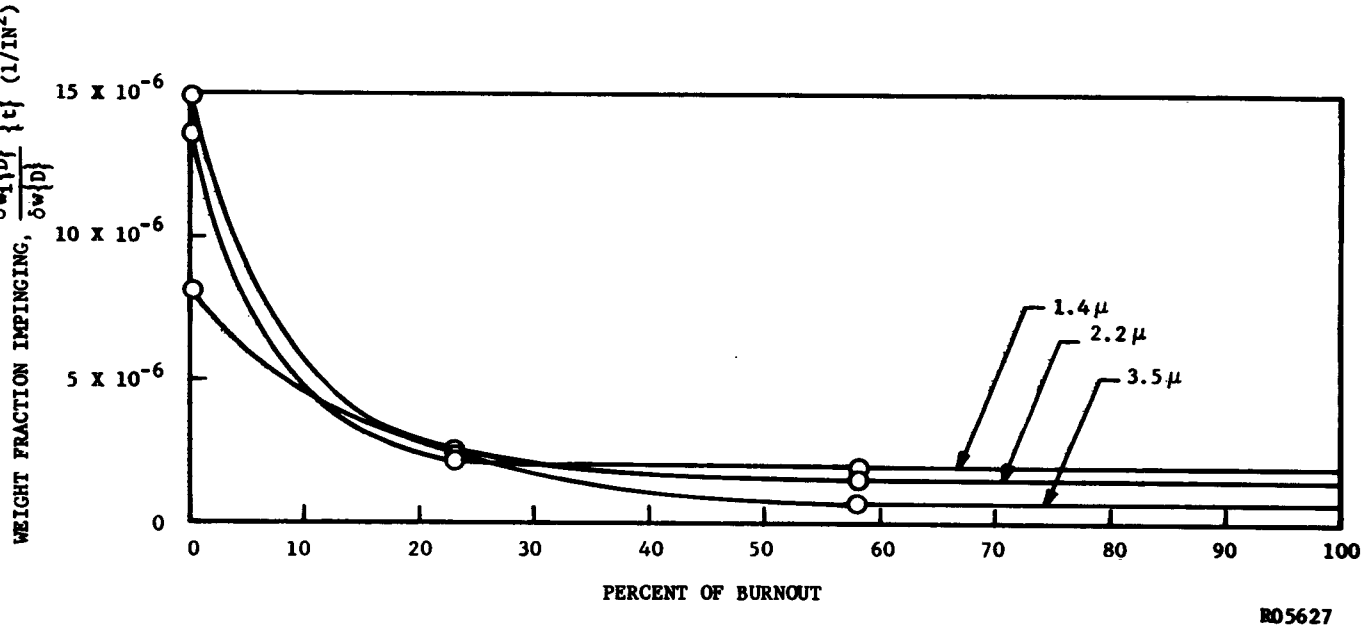

FIGURE 15. WEIGHT FRACTION OF 1.4 μ, 2.2 μ, AND 3.5 μ, PARTICLES IMPINGED AT POINT A VS. PERCENT OF BURNOUT

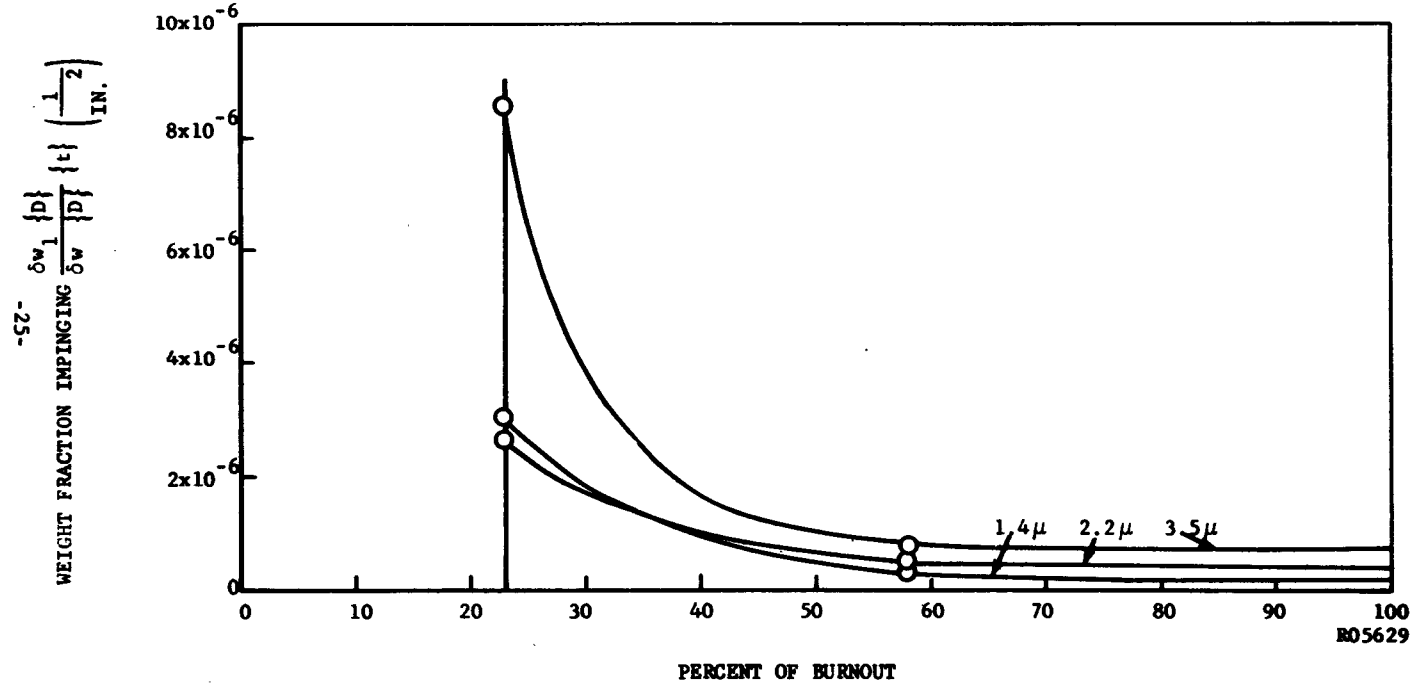

FIGURE 16. WEIGHT FRACTION OF 1.4μ, 2.2μ, AND 3.5μ PARTICLES IMPINGING AT POINT B VS. PERCENT OF BURNOUT

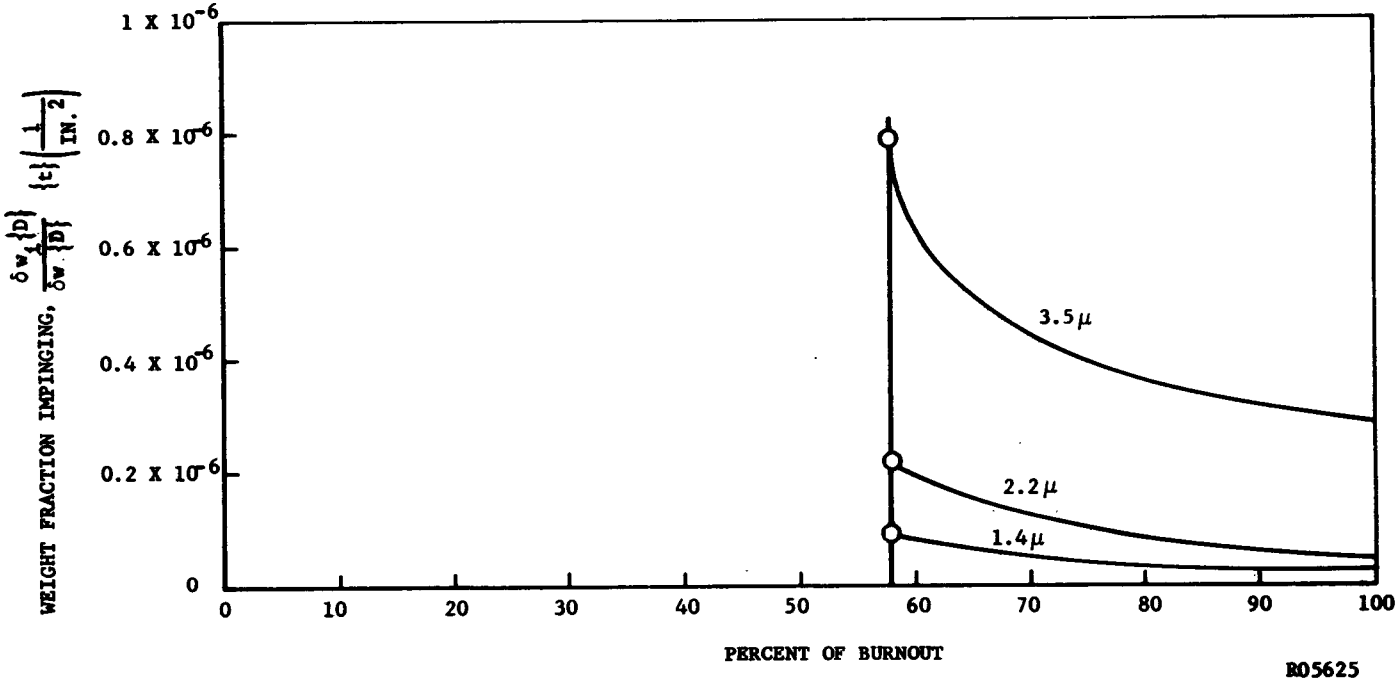

FIGURE 17. WEIGHT FRACTION OF 1.4μ, 2.2μ, AND 3.4μ PARTICLES IMPINGING AT POINT C VS. PERCENT OF BURNOUT

TABLE II

TABULATION OF $\frac{\delta W_i \{D\}}{\delta W \{D\}}$

Point	t_b (% of Burnout)	D (μ)	$\int_{tb}^{100} \frac{\delta W_i \{D\}}{\delta W \{D\}}(t)\, dt$ (% of Burnout)/in^{-2}	$\frac{\delta W_i \{D\}}{\delta W \{D\}}$ $\left(\frac{1}{in^2}\right)$
A	0	1.4	254	2.54
A	0	2.2	285	2.85
A	0	3.5	168	1.68
B	23	1.4	49.6	0.65
B	23	2.2	59	0.77
B	23	3.5	115.4	1.5
C	58	1.4	2.1	0.05
C	58	2.2	4.6	0.115
C	58	3.5	16	0.4

From Table II its possible to obtain $\frac{\delta W_i \{D\}}{\delta W \{D\}}$ as a function of particle size for points A, B, and C. These curves are shown in Fig. 18. As will be explained later, the particle size range we are interested in is from 0.5 μ to 5.5 μ .

The next step is to integrate impingement over the size range of particles found in a rocket. However, to do this the weight fraction of particles as a function of particle size must be known. This function can be obtained by differentiating a curve of Sehgal's[3] data for a 500 psi chamber pressure. The differential of his percent total volume below curve is shown in Fig. 19 with units of the ordinate as $1/\mu$ since

$$\frac{\delta W \{D\}}{W_T} = \frac{d\left(\frac{\delta W \{D\}}{W_T}\right)}{dD}$$

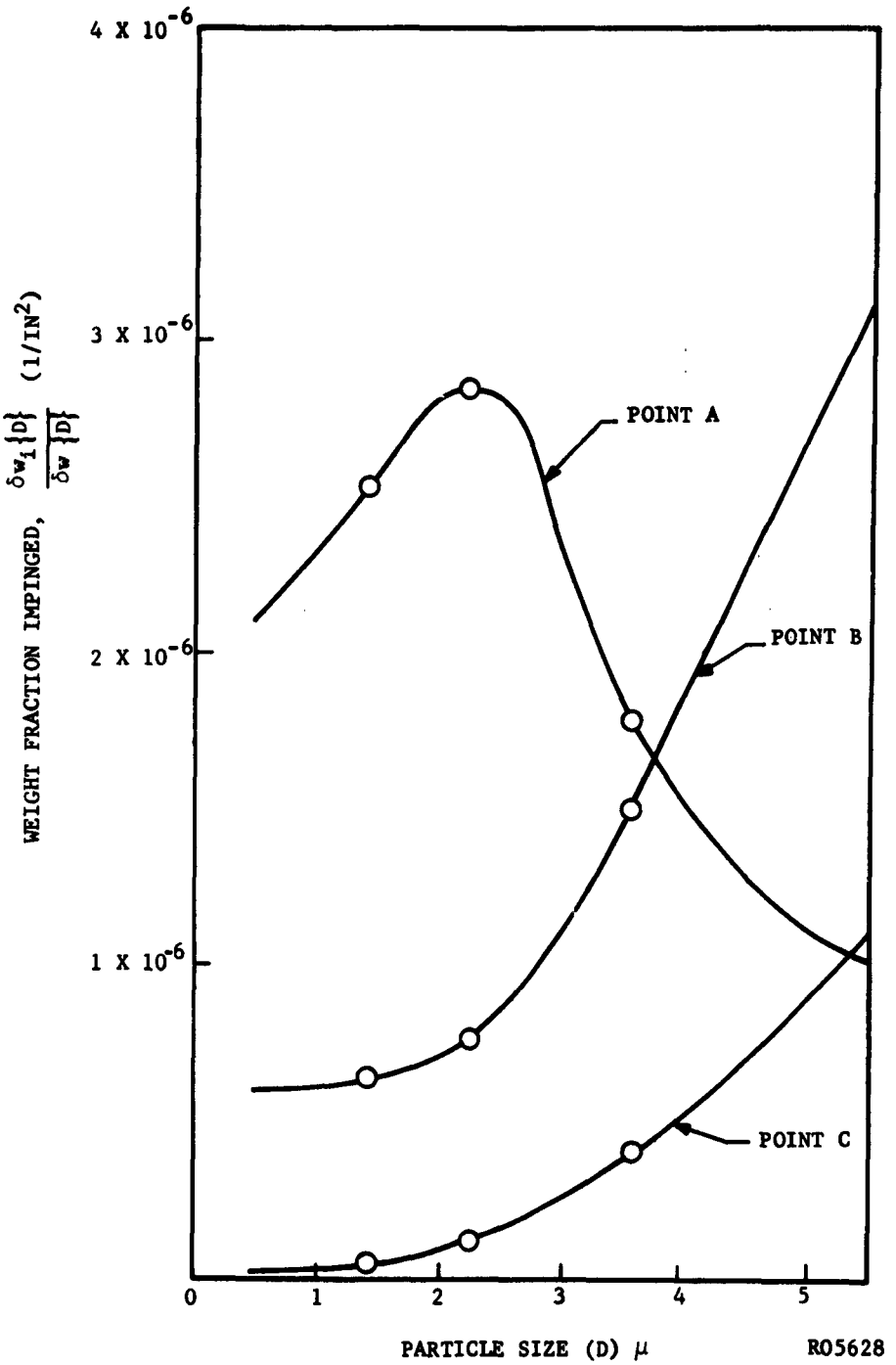

FIGURE 18. AT POINTS A, B, C: ALUMINA WEIGHT FRACTION IMPINGED AS A FUNCTION OF PARTICLE SIZE

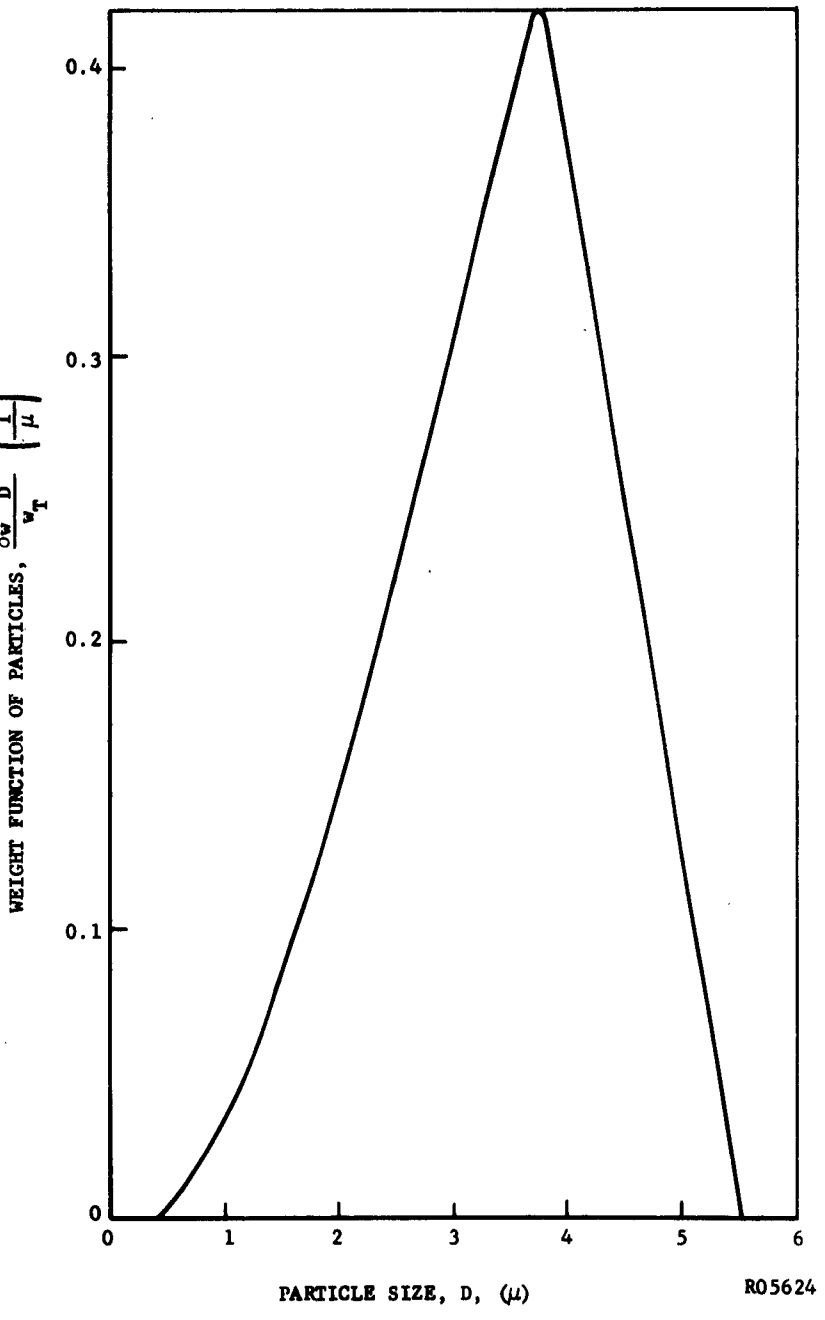

FIGURE 19. PARTICLE SIZE DISTRIBUTION OF ALUMINA SAMPLE OBTAINED FROM MOTOR FIRING AT 500-PSI CHAMBER PRESSURE

where W_T is the total weight of all the allumina particles.

Now by multiplying the ordinate of the curves in Fig. 18 with the ordinate of the curve in Fig. 19 at each particle size and plotting as a function of particle size while still keeping points A, B, and C as parameters, Fig. 20 is obtained. The ordinate of Fig. 20 will be $\frac{\delta W_i \{D\}}{\delta W D} \cdot \frac{\delta W \{D\}}{W_T} = \frac{\delta W_i \{D\}}{W_T}$ with units of $1/\mu$ in^2.

For any one of the three points (A, B, C) it is now possible to integrate impingement over the entire particle size range. The area under these curves can be expressed as:

$$\int_0^\infty \frac{\delta W_i \{D\}}{W_T} \, dD = \frac{W_i}{W_T}$$

which is the weight fraction of alumina that impinged at any point. For a run time of 90 seconds, a burn rate of 500 lb/sec., and 32 percent of the propellant as alumina, the total impingement in lb/sq. in. can be calculated as a function of position.

For example:

$$\text{Impingement} = \frac{W_i}{W_T} \left(\frac{1}{\text{in.}^2}\right) \left(\frac{500 \text{ lb}}{\text{sec.}}\right) (0.32)(90 \text{ sec.})$$

$$= \frac{W_i}{W_T} (14400) \text{lb/sq. in.}$$

This curve for impingement along the nozzle wall integrated for the total firing is shown in Fig. 21. This is the final result desired from the cold-flow modeling test data.

The next step is to convert this data onto a heat flux to the wall, a mechanical erosion effect for such impingement, and a material loss rate from the wall caused by the impingement. Such numbers will be developed and reported in the final report.

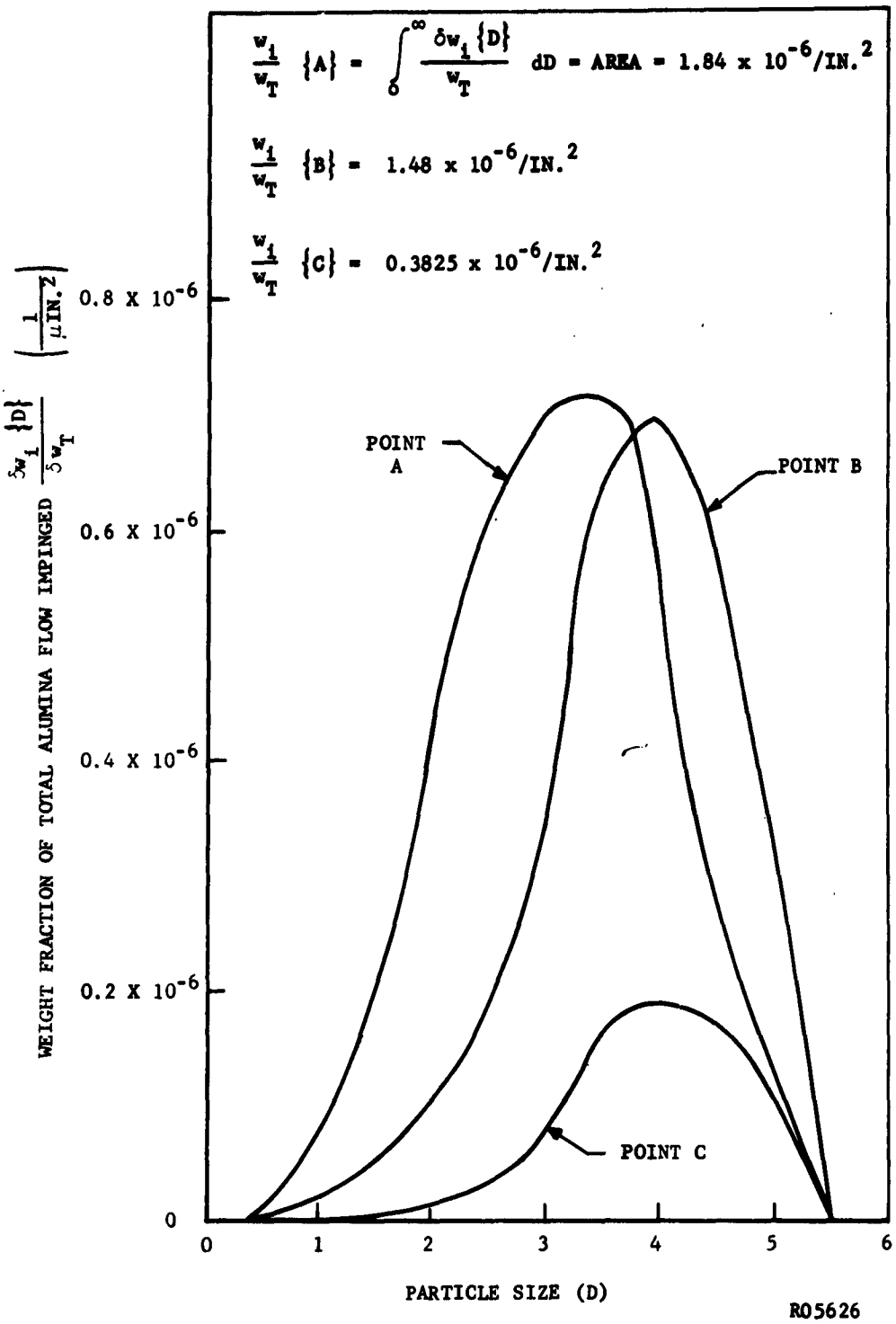

FIGURE 20. WEIGHT FRACTION OF TOTAL ALUMINA FLOW IMPINGED VERSUS PARTICLE SIZE FOR POINTS A, B, AND C.

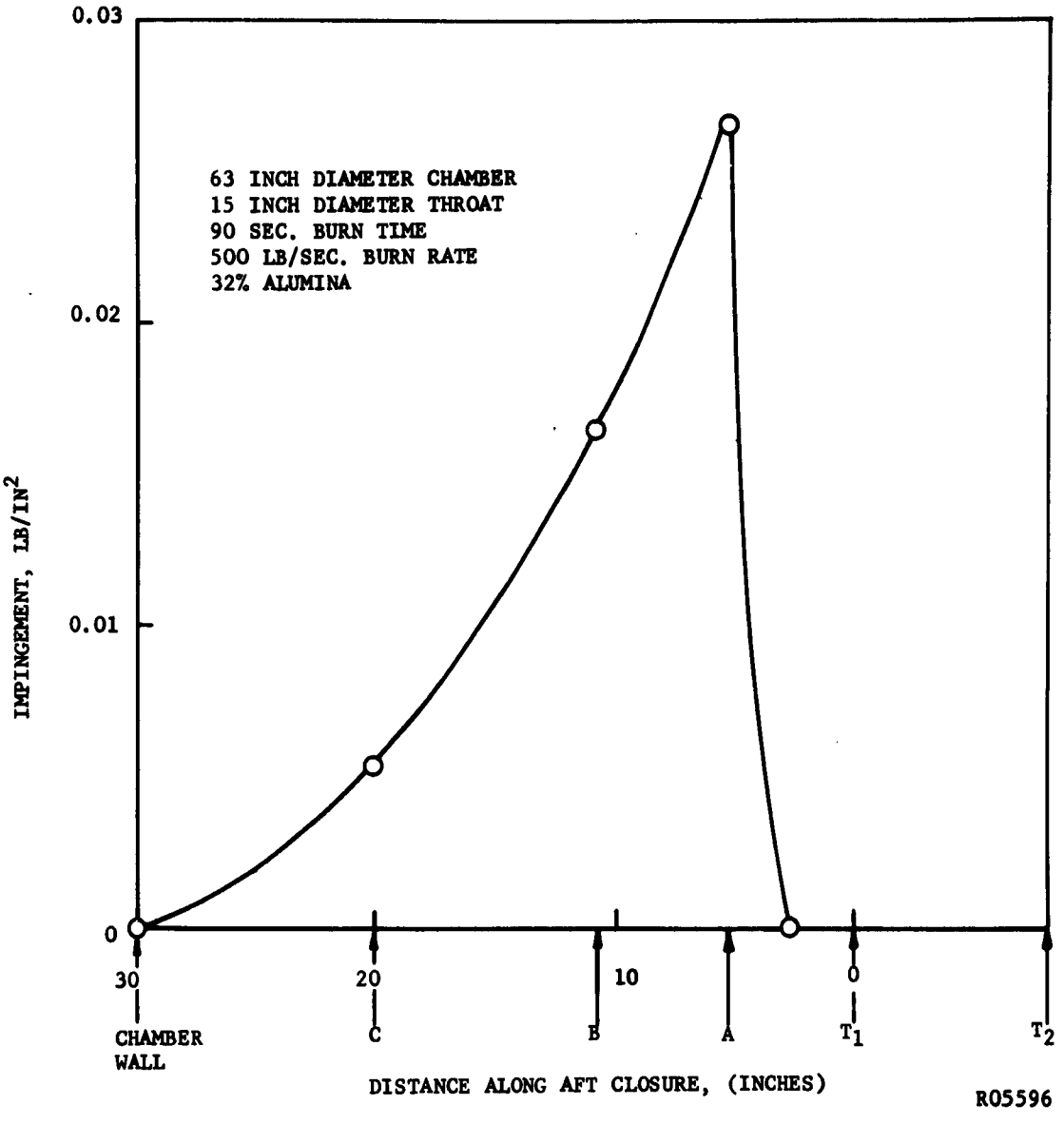

FIGURE 21. TOTAL IMPINGEMENT ALONG ROCKET AFT CLOSURE

SECTION 3

ENGINE TESTING TECHNIQUE DEVELOPMENT

The majority of the engine tests during the third quarter were devoted to a stepwise improvement in the experimental method. Developments in testing technique are listed below:

1. Optimizing radiometer window purge rate:

   Too much nitrogen flow gives the radiometer a lower temperature view; too little purge can result in a dirty window or burned out instrument.

2. Establishing a satisfactory run sequence:

   It was found desirable to have the nozzle preheated for about 2.5 seconds before the slurry flow started. This brought the nozzle peak surface temperatures up to a realistic level of 2500°F. In the case where H_2-O_2-H_2O-Al_2O_3 was fired the H_2O-Al_2O_3 slurry flow was merely delayed. With the system using methanol and aluminum a special preheat hydrogen flow was reduced as the slurry came in.

3. Slurry metering technique improvements:

   Slurry metering at first was accomplished using a position potentiometer on the slurry piston, but when slurry motivation was changed from gas to oil,

the oil flow was then metered since its rate is equal to slurry flow rate.

4. Shut down sequence to avoid slopping slurry onto the nozzle:

Shut down observations of the nozzle deposit were useful in checking whether or not injector performance was even. Also, it revealed if the impinging solids indicated by the thermocouple were adhering or blowing off the surface. In all these cases a shut down with no overshoot of unatomized slurry was desired.

5. Tests of particle loading density across the engine "grain" port:

In several runs an impact bar was placed across the chamber to check for particle flow uniformity. These tests indicated a very even particle distribution. Figure 22 shows the particle impact bar and an alumina impact sample (which was originally found to be uniform all across the bar). The thick bulge of impacted particles within 3/16" of the chamber wall was believed to be a function of the flow conditions caused at the intersection of the bar with the chamber.

6. Surface temperature thermocouple circuit improvements:

The tenuous abrasion-made junction of the surface thermocouples was found to require a high impedence readout circuit with amplification.

7. Slurry preparation and handling techniques and injector modifications to achieve the best possible dispersion of alumina particles in the chamber:

Initially, very heavy nozzle deposits were found after a firing. However, by removing the gel from the slurry and by modifying the injector design to reduce wall

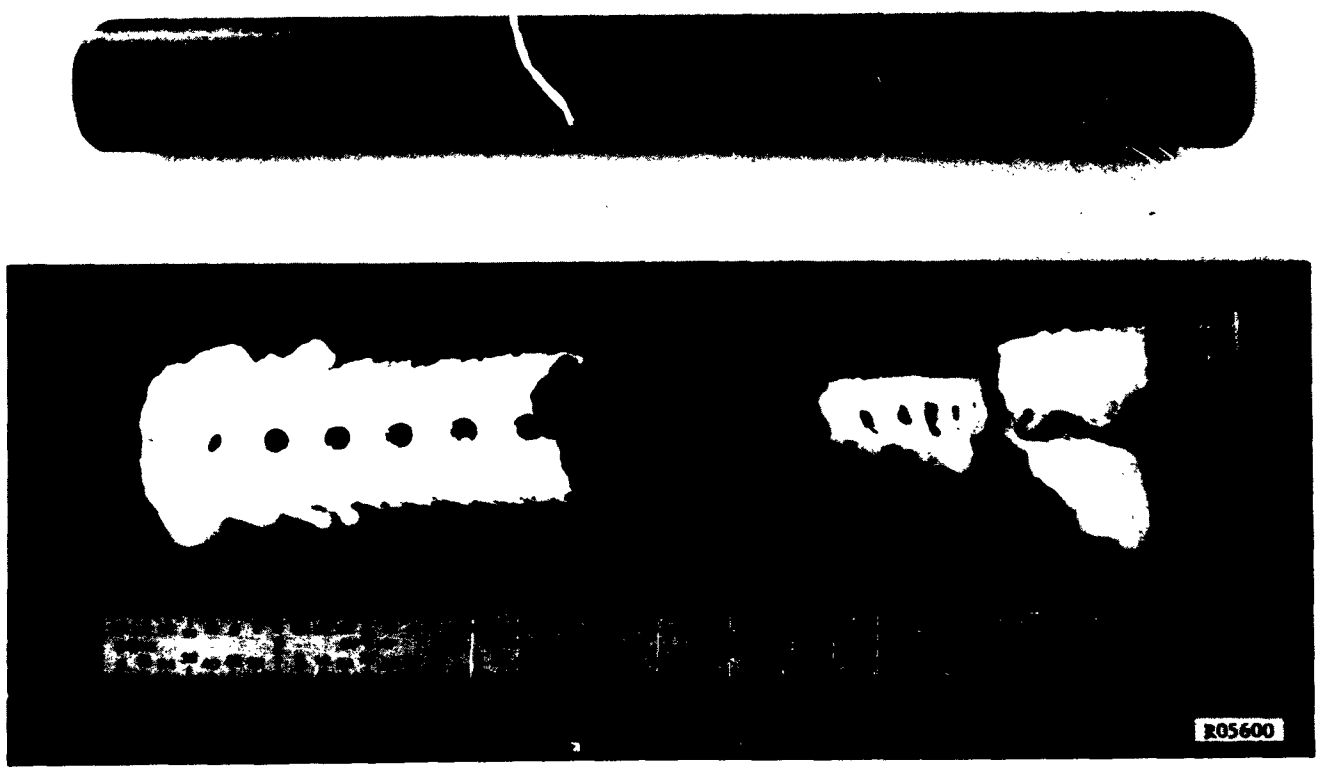

FIGURE 22. MOLYBDENUM CROSS-CHAMBER SAMPLER AND ALUMINA SAMPLE

splashing, the residual impingement was eliminated -- except for the tests where $\emptyset = 0.4$ and where aluminum was actually burned. Thus, improved fineness of dispersion of the solids was achieved. Figures 23, 24 and 25 show nozzle coatings removed after firings. The coatings are not perfectly symmetrical, indicating some need of further injector improvement.

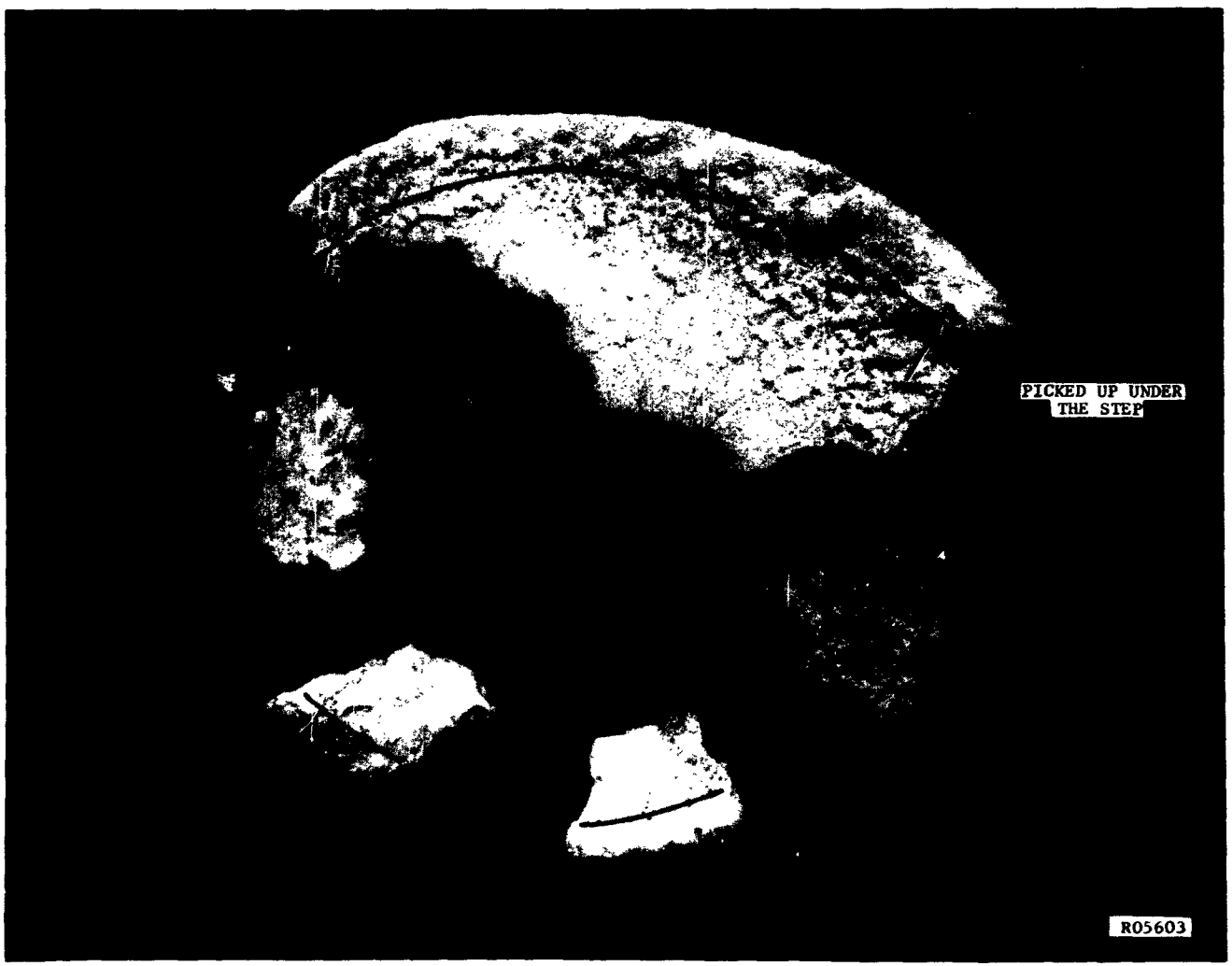

FIGURE 23. NOZZLE ALUMINA DEPOSIT SHOWING HEAVIER DEPOSIT UNDER THE CHAMBER STEP

FIGURE 24. NOZZLE ALUMINA DEPOSIT FROM TEST WITH NO STEP

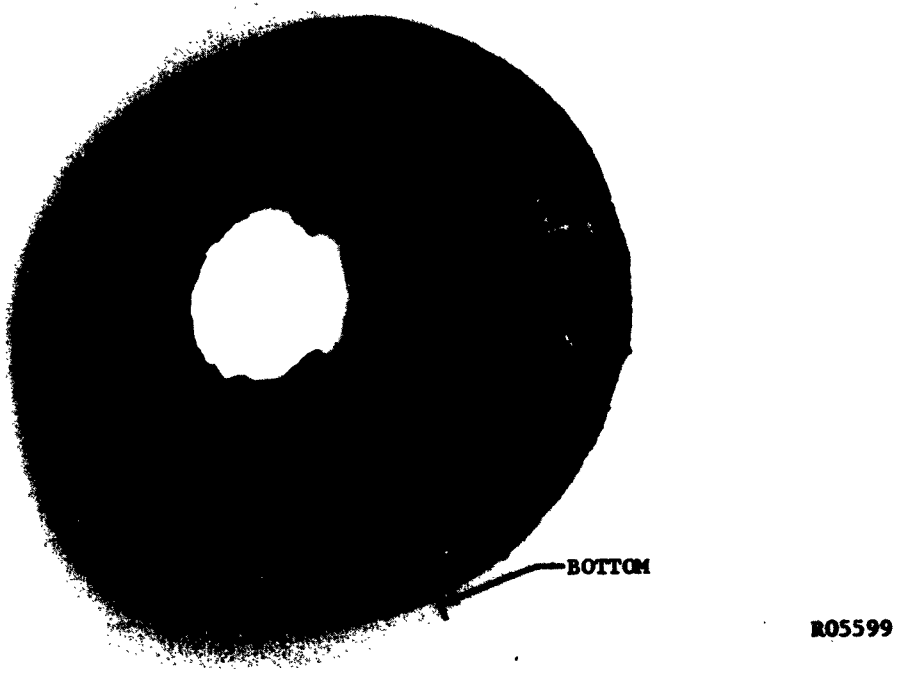

FIGURE 25. NOZZLE ENTRANCE CONE DEPOSIT FROM ALUMINUM-BURNING TEST

SECTION 4

CONDENSED PHASE PARTICLE SIZE IN FIRINGS

Ideally, the nozzle environmental conditions can best be studied if the particle size distribution of the cloud approaching the nozzle is known. Transmission measurements are used to handle this aspect for the particle emissivity determinations, but for impingement a more detailed size analysis is needed.

Under ideal conditions, the particles injected are freely and completely dispersed in the chamber. Injector improvements were made to achieve this as well as possible, but a study to optimize the injector was not attempted. However, steps were taken to determine the particle size distribution of the exhaust cloud from operations with no exit cone. Imperfect dispersion or agglomeration in the chamber could produce larger particles.

Alumina particle sizes in the range of one micron, 1 to 4 microns and 1 to 6 microns were used in the firings. Preliminary samples of exhaust product particles were taken in the center of the plume at thirty feet from the nozzle using an impact sampler. Particle sampling technique improvement will occur when the sampler shown in Figure 26 is used.

Early samples, which may not accurately show all the particle sizes in the cloud, indicate that the burning aluminum produces particle sizes uniformly near one micron in diameter. However, when particles in

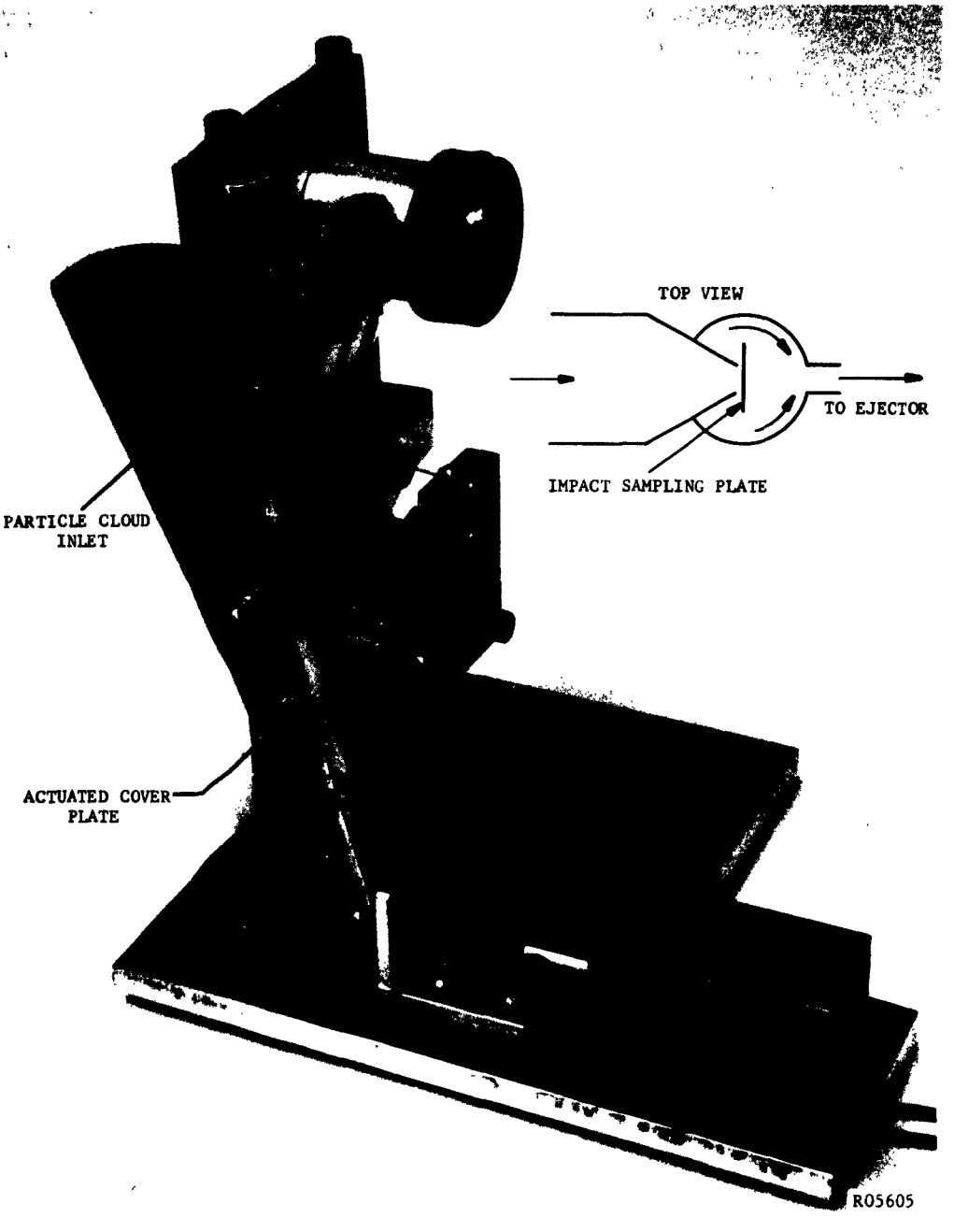

FIGURE 26. EXHAUST CLOUD PARTICLE SAMPLER

the size range of 1 to 4 microns were injected into the engine, the impact samples, photomicrographed in Figure 27, indicated many particles in the size range of 6 to 12 microns. As in other third quarter work these results are qualitative. Improved technique with the new sampler will allow photomicrographs which show the complete particle size distribution in one picture. The new sampler operates with only one fine, high impact slit and with short enough sampling time to yield a sample which can be fully viewed, no layering.

The one micron particles were found to be difficult to disperse in the chamber. Heavy residual nozzle impingement was found on the nozzle after firing. These extra fine, uniform spheres produced a more viscous water suspension.

Originally, a gelling agent was used to make a stable suspension of the alumina particles in water. When this was found to have an adverse effect on dispersion by the injector, the gel was eliminated. The test procedure then became one of pouring the ball milled water dispersion of particles into the run tank, just one minute before the firing. Settling effects were determined to be neglibible in this short time.

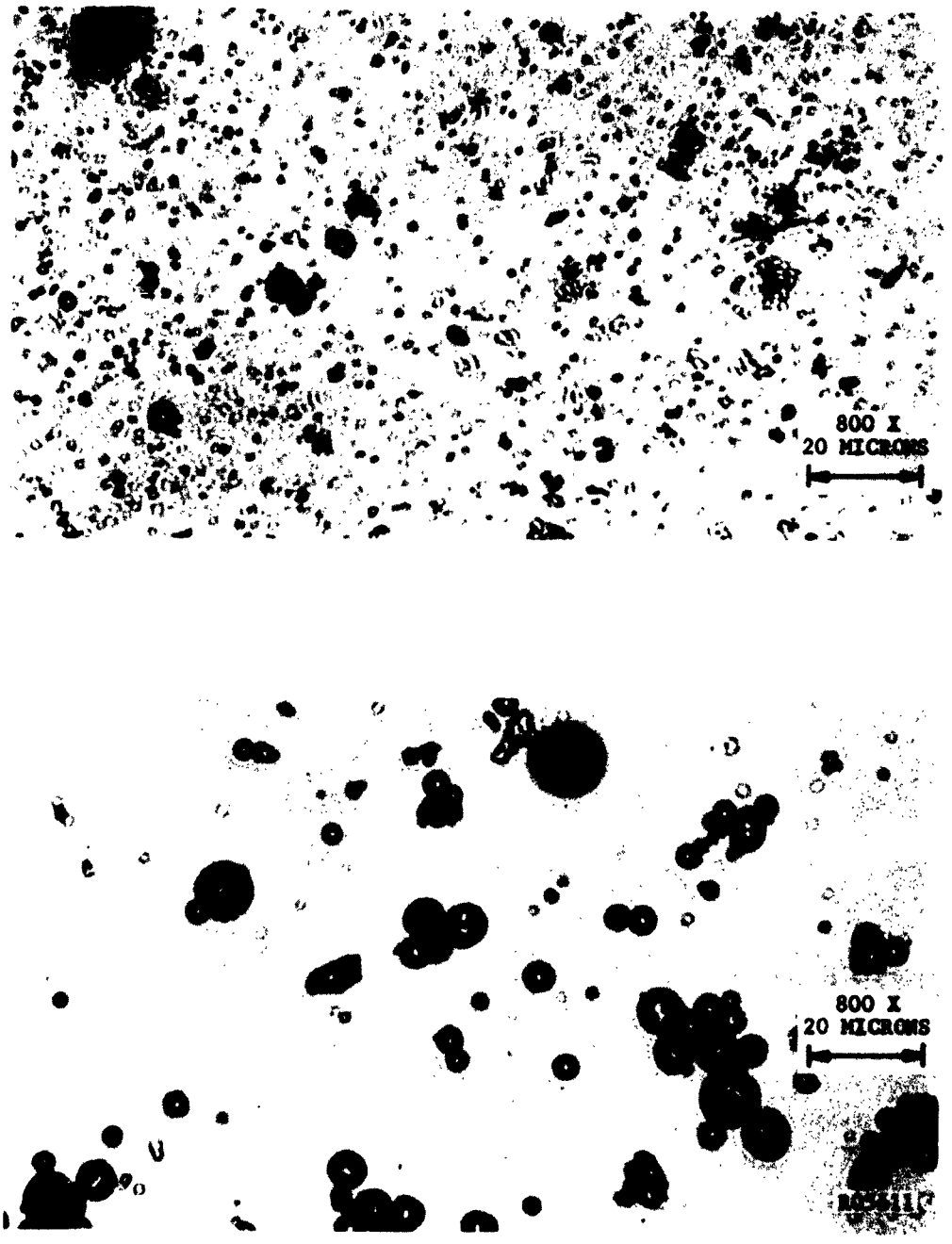

FIGURE 27. COARSEST AND FINEST PARTICLE SIZE FRACTIONS SAMPLED FROM EXHAUST

SECTION 5

NOZZLE HEAT FLUX DETERMINATION

Nozzle heat flux is determined by a transient conduction analysis of the 0.625" thick wall. Outer and inner wall surface temperatures are sensed using Nanmac thermocouples at various points over the nozzle contour. The temperatures are input to a conduction computer program from the Jet Propulsion Laboratory to develop the heat flux values at the nozzle surface.

In a typical test the solids are introduced approximately two seconds after combustion has started. Combustion, with solids flowing, levels out at about 2.6 seconds. The total test duration is 4 seconds.

A total of 39 test firings were conducted during the third quarter. The testing was carried to the point where very interesting data for the heat conduction analysis were developed. A number of tests were analyzed and these results are shown below. The results are preliminary; data from more refined operations are forthcoming.

Figure 28 shows the distribution of thermocouple locations on the molybdenum nozzle. Figures 29 through 31 show surface heat flux histories at the various locations of the thermocouples for tests fired with no condensed phase, with a melted alumina phase and with an unmelted zirconia phase. Chamber temperatures are approximately the same in all cases, about 5200^{o}F.

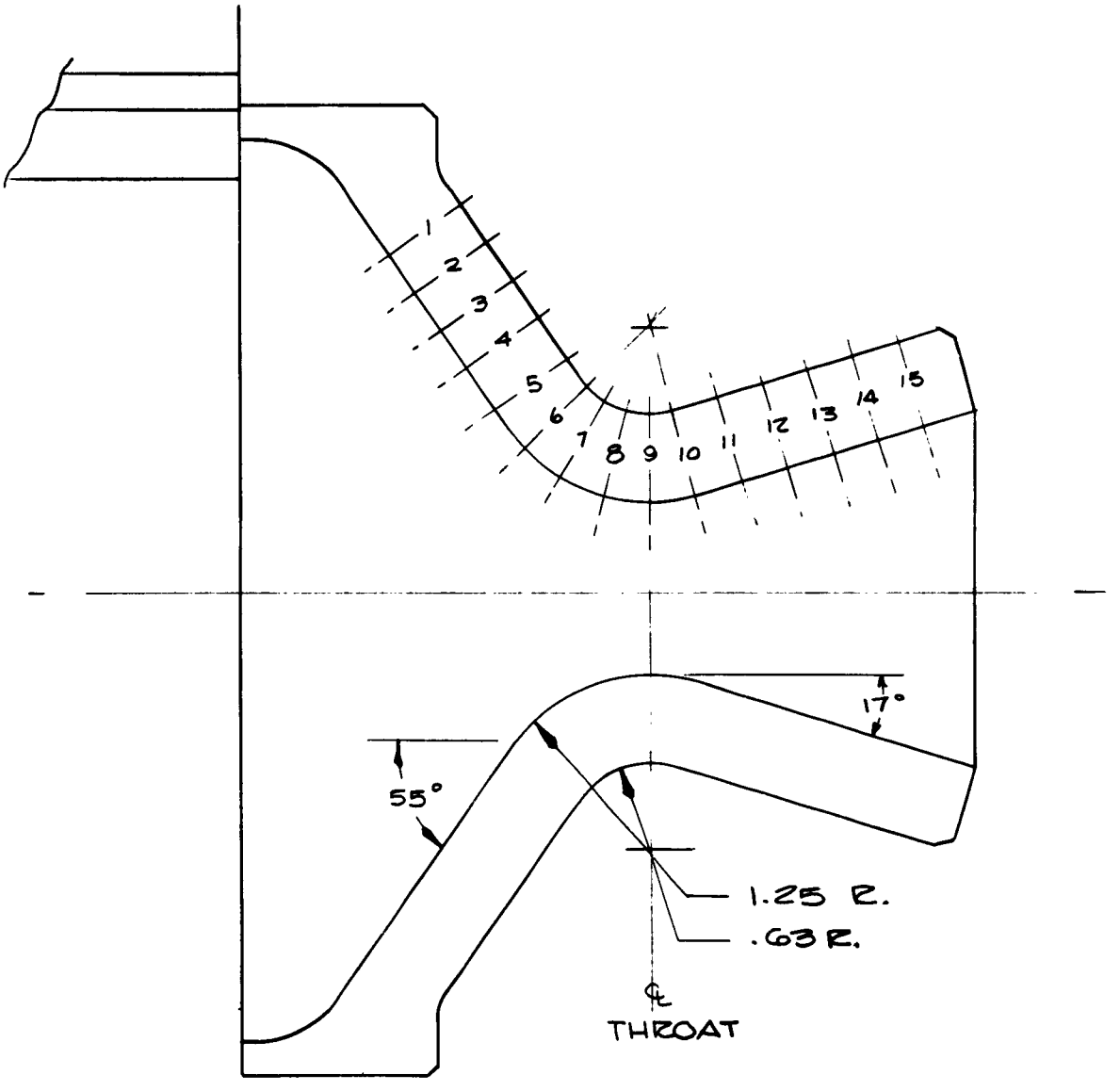

FIGURE 28. SURFACE THERMOCOUPLE LOCATIONS

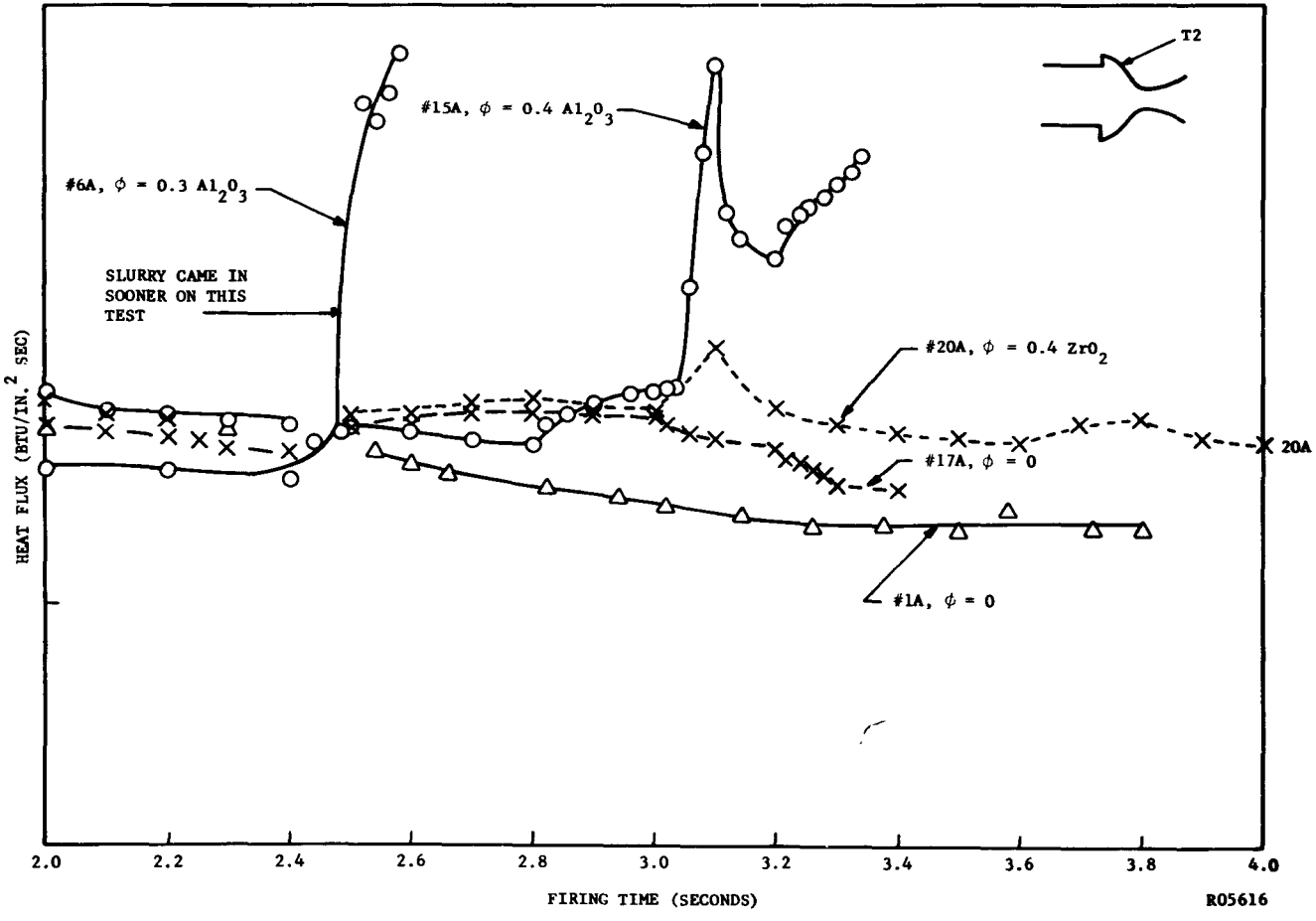

FIGURE 29. NOZZLE HEAT FLUX AT POSITION 2

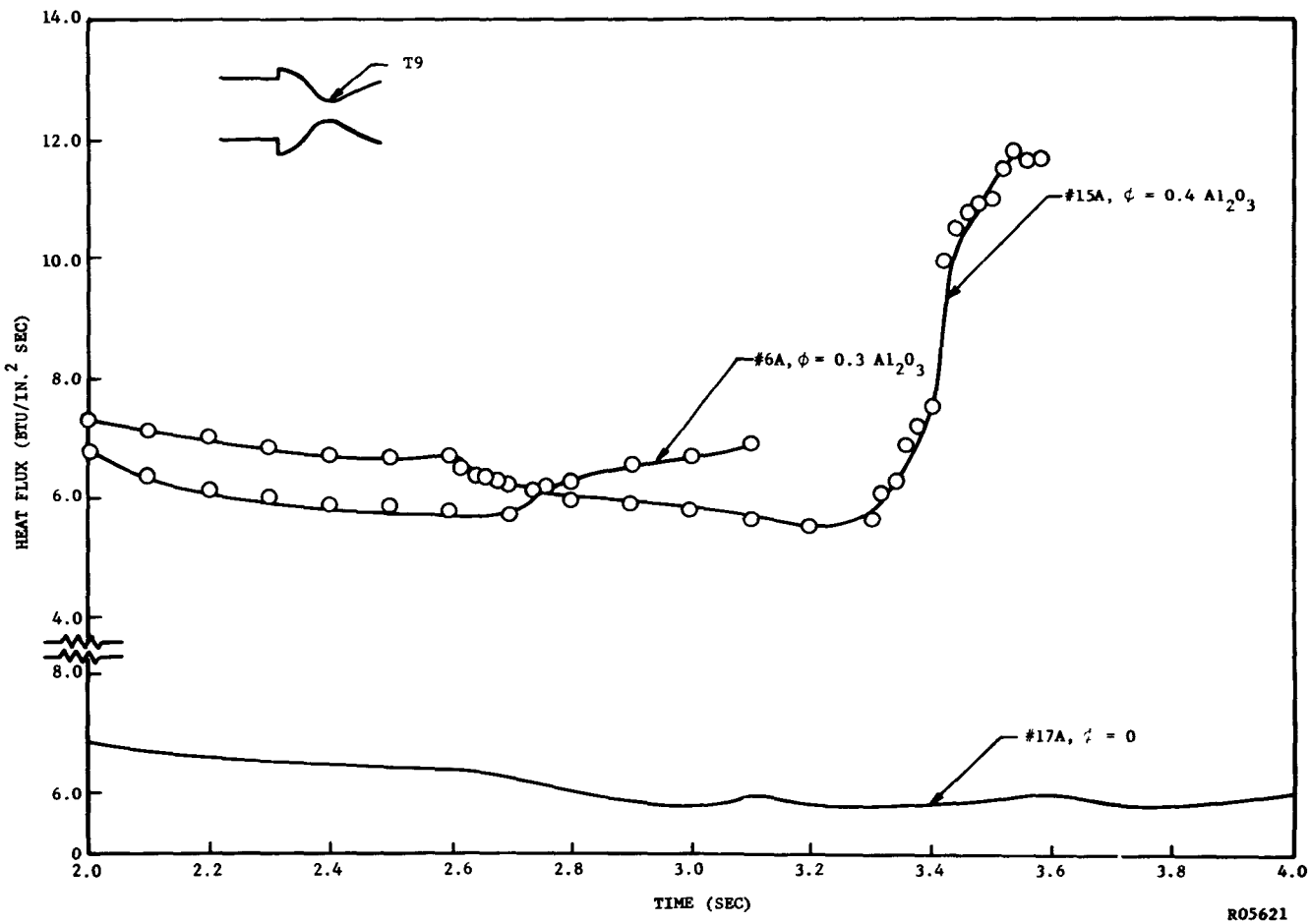

FIGURE 30. NOZZLE HEAT FLUX AT POSITION 9

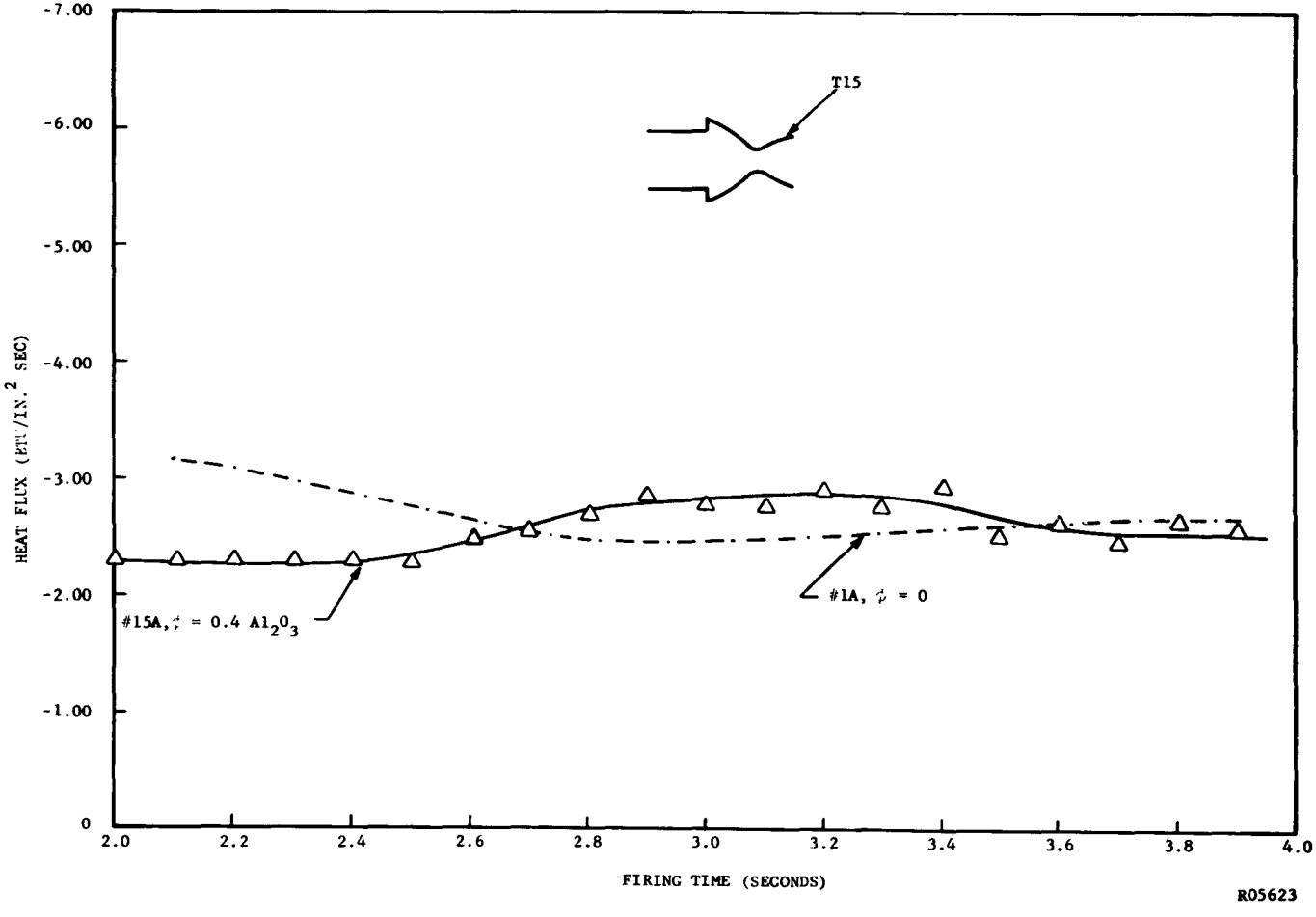

FIGURE 31. NOZZLE HEAT FLUX AT POSITION 15

It can be seen how the condensed liquid alumina causes a drastic heating flux rise until it coats the wall and insulates it. In most cases when the temperature or heat flux drops, after impingement, the computation was stopped. The "dry" unmelted zirconia has much less effect on the heat flux than does the molten alumina.

Figure 32 shows the heat transfer coefficient proceeding through the nozzle. These are based on the wall temperature value and the theoretical chamber gas static temperature, less a 500°F estimated temperature drop due to heat loss to the large chamber. The shape of the curves for clean gas resemble those compiled by various people for "clean" liquid propellant firings. Actual convective coefficients for this test data will be computed and compared with the "clean gas" data. However, these first test data are from tests with only rough control of propellant flow rates.

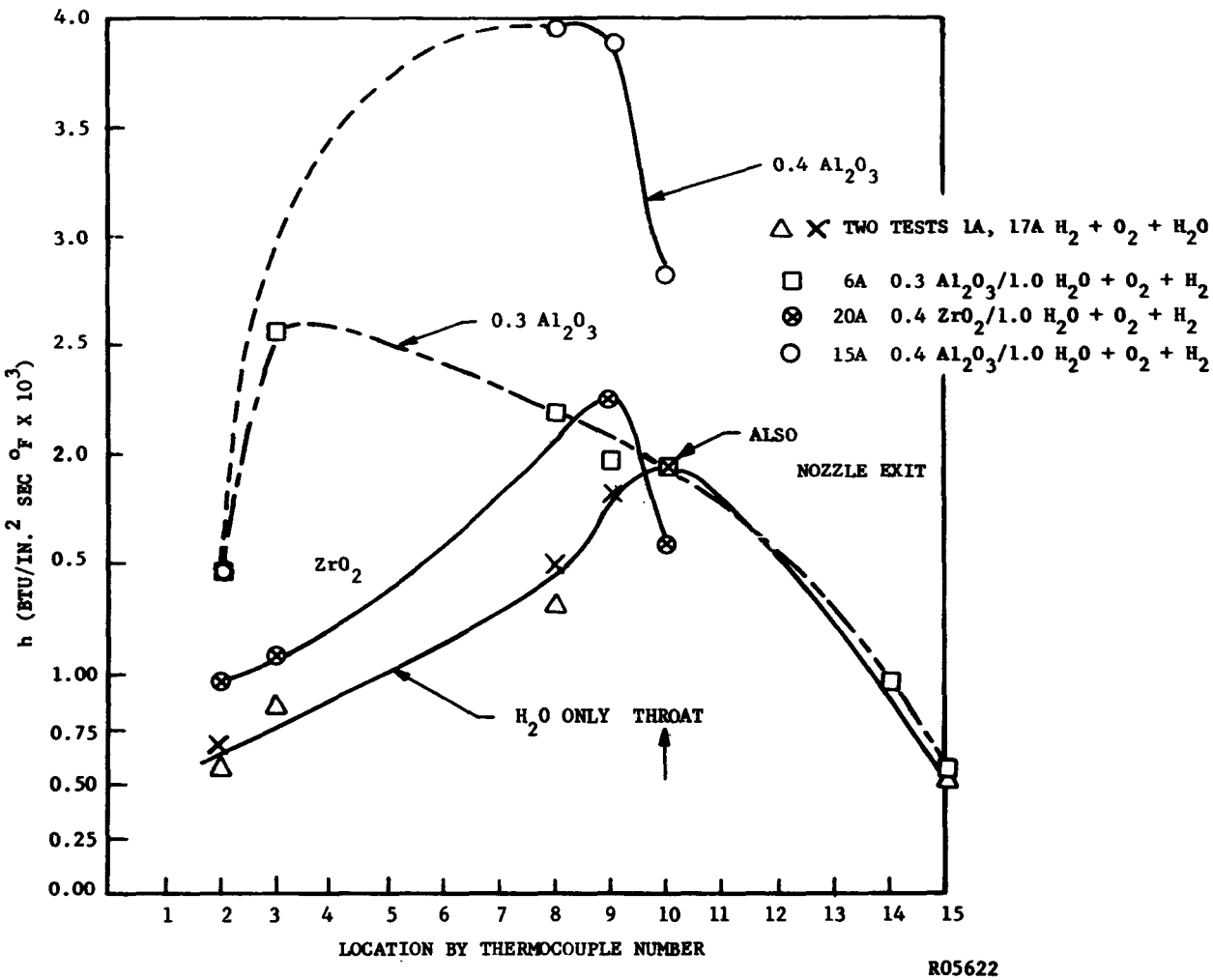

FIGURE 32. NOZZLE HEAT TRANSFER COEFFICIENTS VS. POSITION WITH VARIOUS CONDENSED PHASES PRESENT

SECTION 6

THE INFRARED RAPID-SCAN SPECTROMETER

In order to provide the instrumentation requirements of the needs for the radiation study contract, the Philco Research Laboratories have developed a scanning spectrometer system. The final stages of fabrication and installation of the rapid-scan spectrometer system were completed during the third quarter. The effects of the nitrogen atmosphere on the performance of the equipment were examined and found to be satisfactory. Removal of atmospheric absorption bands, in particular those due to water and CO_2 molecules, was found to be quite efficient and facilitated the interpretation of observed spectra. A preliminary wavelength calibration was determined for the system and the resolution capabilities were obtained at a few wavelengths. A number of check runs were made in order to obtain a feeling for the sensitivity of the equipment as a function of the locations along the engine at which future data runs will be made (primarily the chamber and throat locations). Optical transmission measurements in the 1 to 2.8 micron wavelength range were made by introducing a tungsten ribbon filament lamp into the system.

6.1 OPTICAL SYSTEM

The design and fabrication of a rocket flame imaging system was completed and its installation is shown in Fig. 33, 34, and 35. The horizontal periscopic configuration was employed in order to removed the spectrometer and associated electronic equipment from the immediate vicinity of the rocket engine. Placement of the equipment behind a protective wall eliminates the possibility of damage from the ever present dangers of destructive firings. Since a relatively long pathlength (about 15 feet) was then necessary, absorption of the radiated flame energy by atmospheric constituents became a problem. In the wavelength region under study (1 to 5 microns), the principal absorption bands are from H_2O molecules (these being centered about 1.38, 1.87, 2.7, and 3.2μ) and from CO_2 molecules (with bands centered about 2.7 and 4.3μ).[4] In order to eliminate this effect, the entire optical path, from engine to spectrometer, was encased in a closed container with facilities for purging with dry nitrogen gas, thereby replacing the normal atmosphere with a non-absorbing one.

Figure 36 shows the atmospheric transmitted emission spectrum of a tungsten ribbon filament lamp in the wavelength range of 1 to 3.0μ (energy emitted beyond those wavelengths is not observed due to the total absorption by the glass envelope). The appropriate bands are labeled and show the effect which they produce on the spectrum. The large dip at 1.38μ is especially important, because this is approximately the wavelength for peak emission of a blackbody at about 4500°F. Since this is representative of the temperatures encountered in motor firings, considerable detail could be lost from the flame emission spectra. Figure 37 shows absorption of the emission spectrum of 1832°F blackbody radiation source. This spectrum shows in greater detail the absorption due to atmospheric constituents, H_2O at 2.7μ and CO_2 at 4.3μ. Figure 38 shows the same blackbody spectrum when utilizing the nitrogen atmosphere. Note that the absorption bands are now nearly non-existent. The small ripples that remain at the appropriate wavelengths are

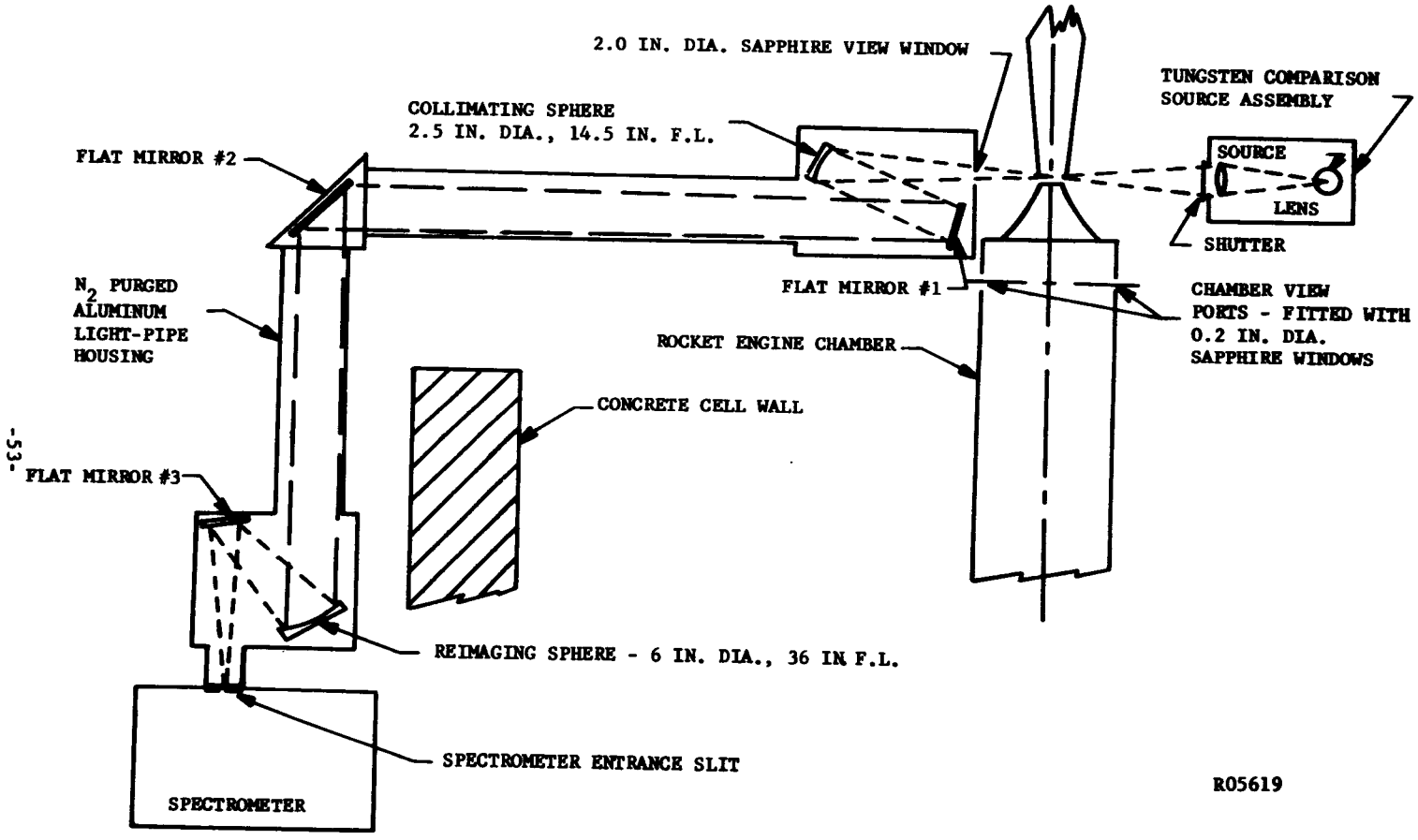

FIGURE 33. ROCKET FLAME IMAGING SYSTEM

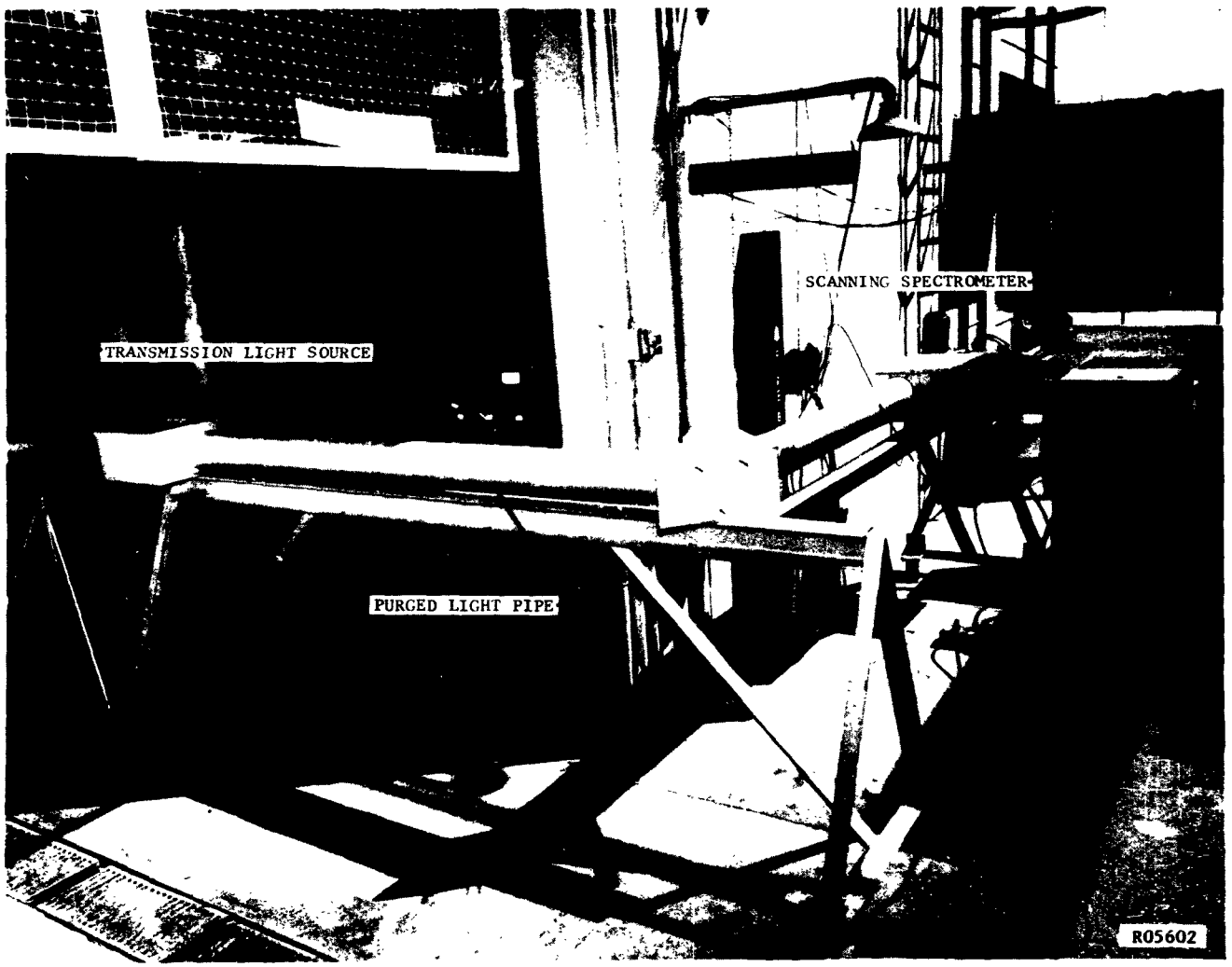

FIGURE 34. TEST CELL SET-UP FOR RADIATION ANALYSIS

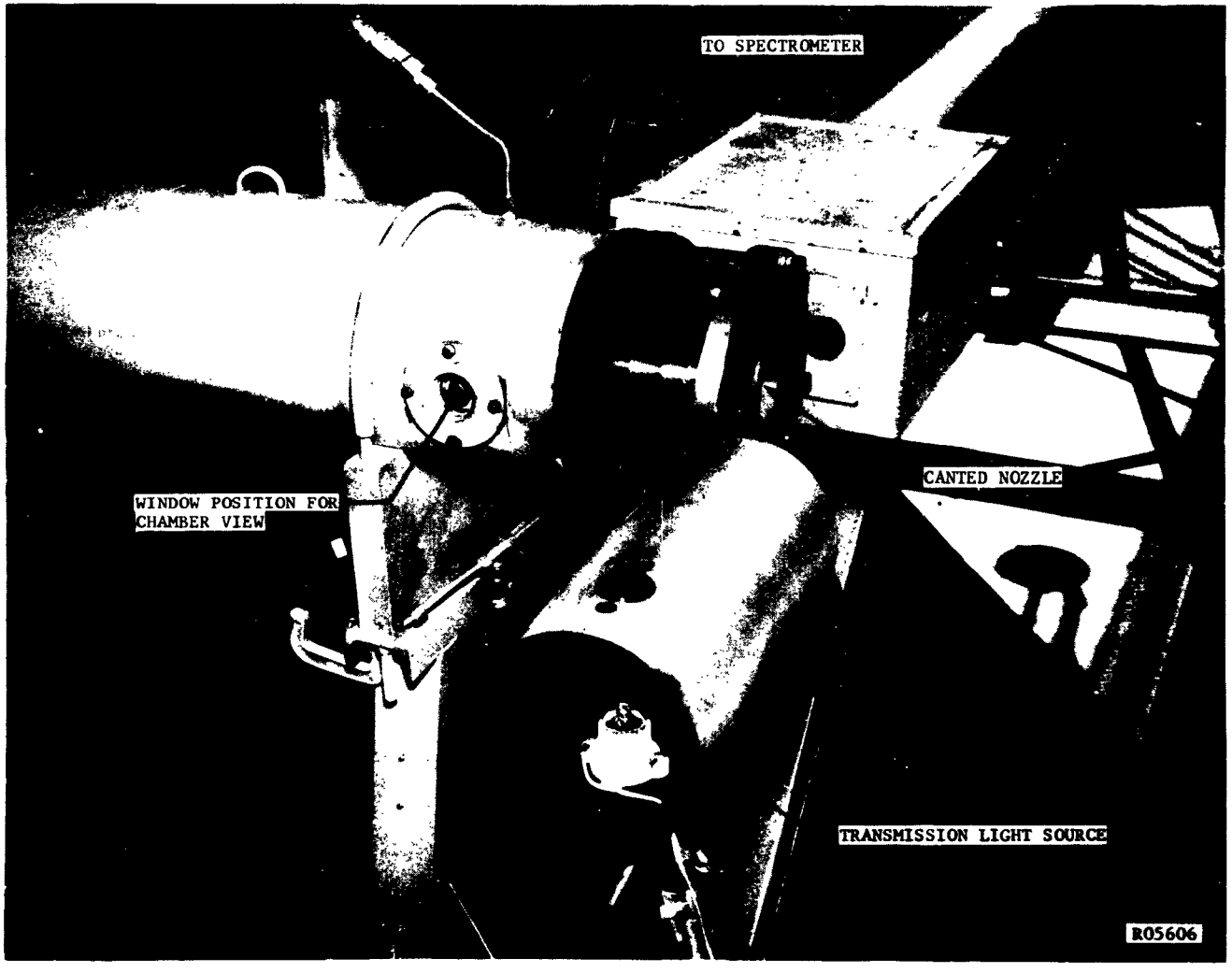

FIGURE 35. ENGINE AND SPECTROMETER ACCESSORIES

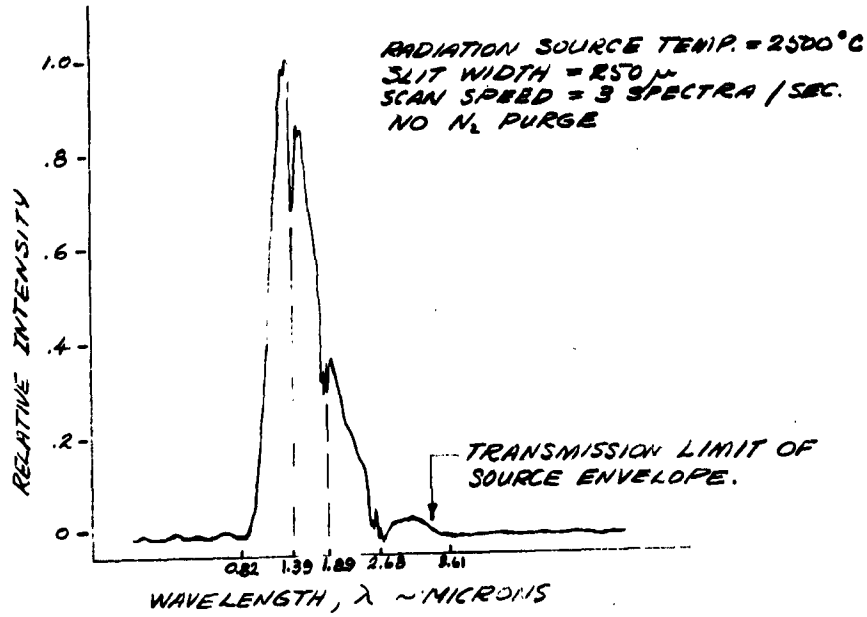

FIGURE 36. RELATIVE SPECTRAL RADIANCY OF A TUNGSTEN RIBBON FILAMENT LAMP SHOWING ATMOSPHERIC ABSORPTION BANDS

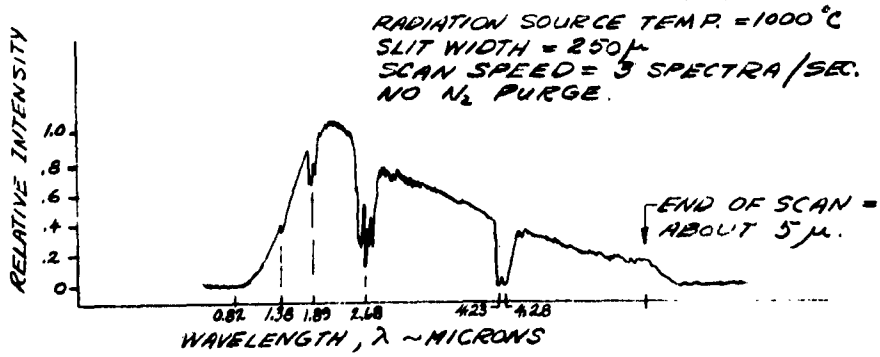

FIGURE 37. RELATIVE SPECTRAL RADIANCY OF BLACKBODY SOURCE SHOWING ATMOSPHERIC ABSORPTION BANDS

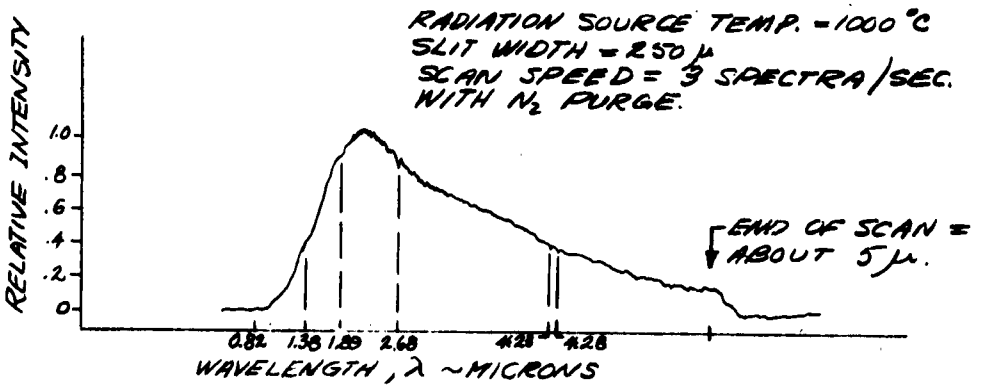

FIGURE 38. RELATIVE SPECTRAL RADIANCY OF BLACKBODY SOURCE WITH OPTICS IN NITROGEN ATMOSPHERE

due to the short atmospheric pathlength between the radiation source and the front of the nitrogen atmosphere container. In actual operation even the smallest absorbing paths will be purged with nitrogen and all such effects should be eliminated.

The optical imaging system was made as simple and as rugged as possible. Although the optical bench was made of an extremely sturdy construction,it is nevertheless quite mobile (see Figure 34). The stand is fitted at six locations with casters which provide the mobility. When the equipment is in use, adjustable legs are lowered to support the stand, thereby raising the casters off the ground. Figure 39 is a photograph of the spectrometer and associated controls. The spectrometer is purged with nitrogen at the location shown in the photograph. Another purge inlet is provided at the motor end of the light-pipe. No attempt at making the system completely air tight was made, but leaks were kept at a minimum so that low nitrogen flow rates could be used.

Also shown in Figure 35 is the tungsten ribbon filament comparison source and focusing optics. The source is focused at the exact position in the flame at which the spectrometer entrance mirror is focused. It is used to make optical transmission measurements on the flame. In particular, it is desired to measure that amount of the comparison source radiation which is absorbed during the firing by the hot particulate matter. Generally these would be alumina, or carbon particles. In work performed for the Allegheny Ballistics Laboratory, Dobbins[5] has shown that an average particle size can be specified for a cloud of flowing gas and particles if an accurate measurement of the optical transmission through the cloud can be made. Preliminary measurements on the experimental equipment constructed at Philco Research Laboratories show that measurements can be made at infrared wavelengths. One difficulty may arise if flame temperatures in the chamber are sufficiently high to prohibit the radiation from the comparison source from being seen by the detector. In this event a brighter source may have to be located.

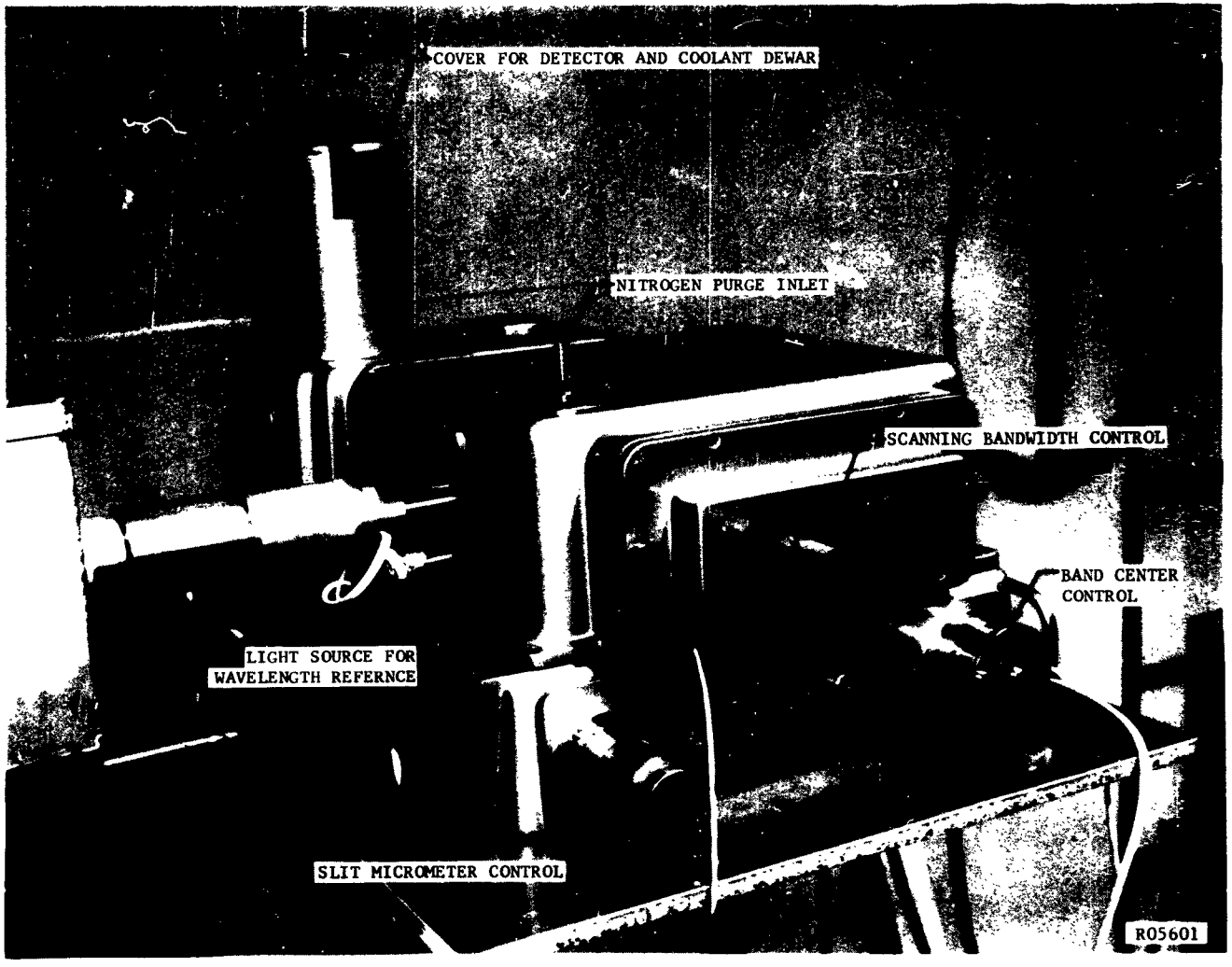

FIGURE 39. RAPID-SCAN SPECTROMETER ATTACHED TO LIGHT PIPE

The transmission measurement technique is as follows. A record of the emission of the comparison source is obtained prior to the run. This is done with a lamp current such as to provide a signal large enough to be viewed through the flame. During the run, a record is made of the emission from the particle-containing flame, this being done without radiation from the comparison source. After a short time a shutter in front of the comparison source is opened and the total radiation spectrum (that is, the simultaneous lamp plus flame emission) is recorded also. If, at a given wavelength we designate "A" the recorder deflection due to the lamp only, "B" the deflection due to the flame only, and "B+C" the deflection due to the lamp plus the flame, then we have all of the necessary factors for the transmission measurements. If the quantity "B" is subtracted from the "B+C" measurement, we have the amount "C" which is the radiancy from the comparison source which was transmitted through the flame. The amount of energy absorbed is then

$$\alpha = \frac{A - C}{A} = 1 - \frac{C}{A} \tag{1}$$

or the amount transmitted is

$$\tau = 1 - \alpha = \frac{C}{A} \tag{2}$$

Note that it is not necessary to know the temperature, or to evaluate the radiancy of the comparison source. All that is needed is the magnitudes of the relevant deflections

6.2 CHECK RUNS

A number of runs was made in order to evaluate the operating parameters of the spectrometer for future data runs. Of primary concern was instrument sensitivity as a function of slit width and amplifier gain for a number of run conditions. That is, runs were made using a gas only

(H_2-O_2) system, a gas plus alumina particles system, and carbon containing systems. By experimenting with these systems, it was felt that more accurate estimates of the instrument settings could be made in future data runs, thereby maximizing the percentage of useful firings. Since final radiancy calibrations have not yet been completed, the sample runs presented will represent only qualitative information at the present, but will be re-evaluated for quantitative values later.

A firing sequence was adopted in which it was possible to evaluate all radiation modes during each run. That is, each firing presented information regarding gas only emission, gas plus particulate emission, and comparison source transmission. The figure below is a schematic representation of a typical firing sequence. Total run durations are generally of the order of 5 to 6 seconds, and proportionately divided as shown.

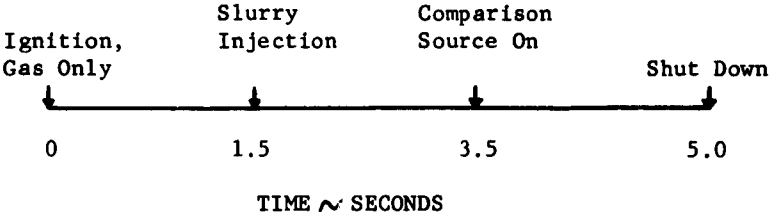

Figure40 is the emission spectrum obtained at the throat for H_2-O_2 engine firing. Since Kirchoff's Law equates the emissivity to the absorptivity for a blackbody, or less specifically, states that a good absorber is good emitter[6], we would expect a good deal of emission from water and CO_2 at the wavelengths for which we observed absorption of our comparison sources. We see in the abovementioned spectrum that emission bands do in fact exist about the proper wavelengths. These bands are broad enough (due perhaps to flame broadening) that a certain amount of self absorption is evident. This is particularly evident in the strong 2.7μ band. There is little or no evidence of any continuum emission in this spectrum, and radiation beyond

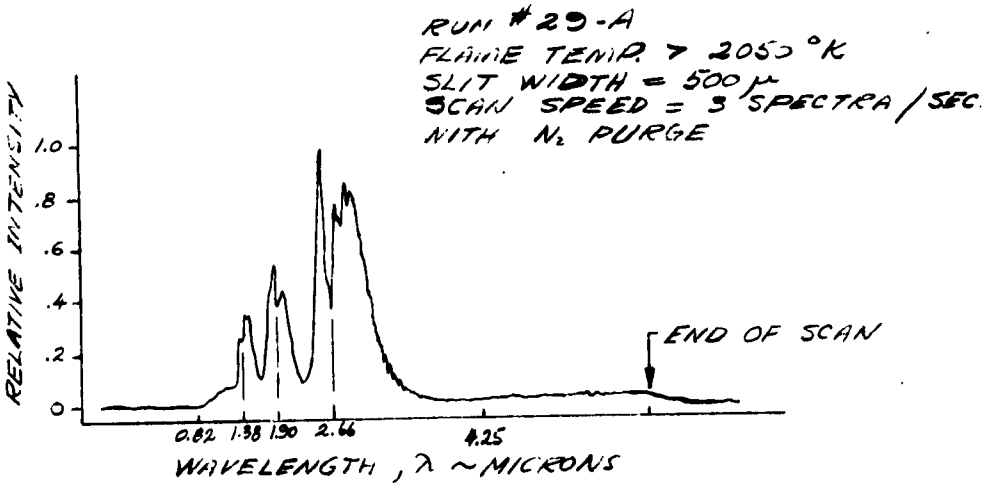

FIGURE 40. SPECTRUM OF H_2 - O_2 FLAME

about 3μ was either non-existent or of such a low level as to be immeasurable. A striking contrast to this spectrum is shown in Figure 41 in which a strong emission band centered about the 4.3μ CO_2 band is seen. This spectrum was obtained during the portion of the run in which benzene (C_6H_6) was introduced. Note that in the 1 to 3μ region the spectrum is nearly identical to that for the gas only system, the primary difference being mainly one of amplitude. This is to be expected, however, since the introduction of the benzene reduced the flame temperature. There is still apparently little or no evidence of continuum emission present. A final change to the original spectrum is shown in Figure 42, which shows the effect of introducing a continuum spectrum (in this case from the tungsten ribbon filament lamp) upon the existing spectrum. Since the emission from the lamp is of such a low level $\left(\frac{I_{\lambda,T}}{I_T(max)} = 1/5\right.$, where $I_{\lambda,T}$ is the spectral emission at a given temperature and wavelength and $I_T(max)$ is the peak emission at the same temperature and at the wavelength for peak emission$\left.\right)$ compared to the 2.7μ H_2O emission band it is seen that that portion of the spectrum (2.7μ) appears practically unchanged.

Of primary interest are the spectral characteristics of an alumina-containing flame. A typical test run is shown in Figure 43. The conditions were for $\phi = 0.2$ ($\phi = \dot{w}_p/\dot{w}_g$, where $\dot{w}_p$ is the mass flow rate of particles in the flame and $\dot{w}_g$ is the flow rate of all gaseous constituents in the flame) and a flame temperature of about 2050°K. The gas only spectrum for that run has been included in Figure 44 in order to show the relative intensity of the continuum emission. Since no carbon containing material was present in the propellant (slurry consisted only of Al_2O_3 powder suspended in distilled H_2O) it is assumed that this radiant emission was produced by the hot alumina in the flame. The relatively low temperature was obtained because the radiancy measurements were made at the throat section of the motor.

6.3 CALIBRATIONS AND RESOLUTIONS

There are two simple methods of calibrating an infrared spectrometer for wavelength position. The easiest method consists of using extremely

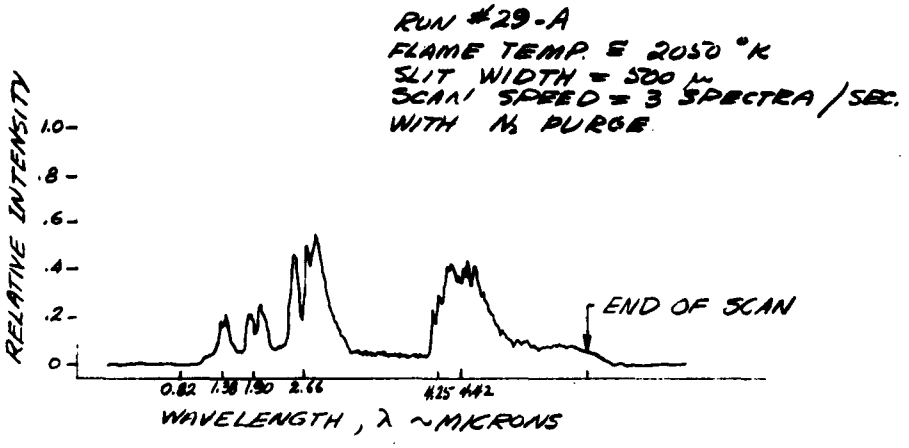

FIGURE 41. SPECTRUM OF BENZENE (C_6H_6) BURNING IN A H_2 -O_2 FLAME

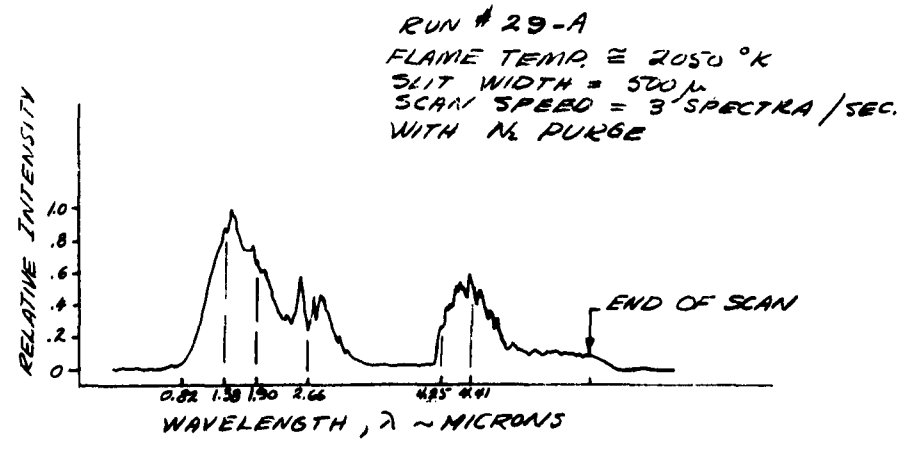

FIGURE 42. SPECTRUM OF H_2-O_2-BENZENE FLAME WITH TUNGSTEN COMPARISON SOURCE SUPERIMPOSED

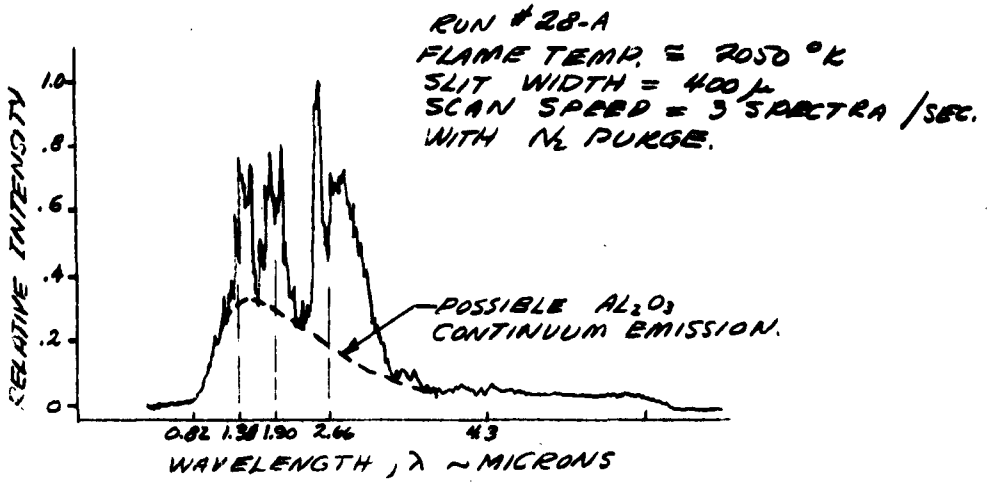

FIGURE 43. SPECTRUM OF ALUMINA CONTAINING H_2-O_2 FLAME

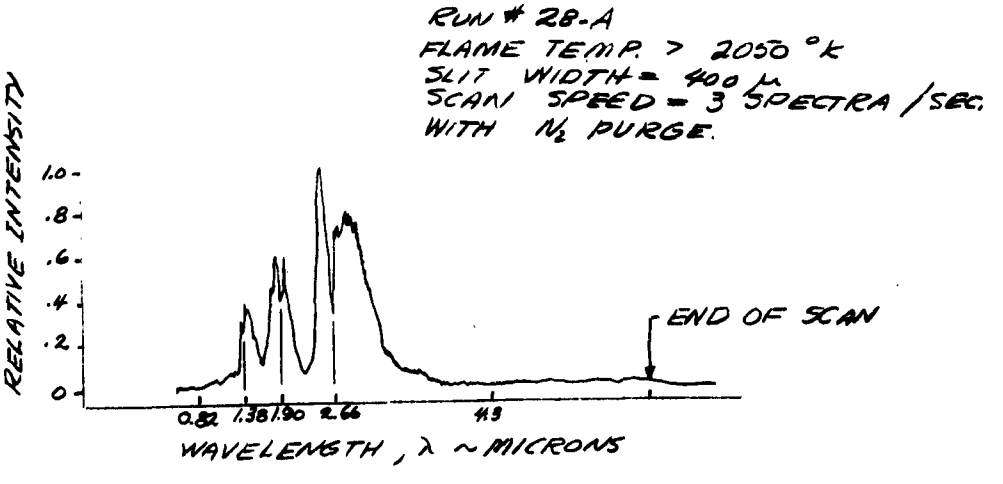

FIGURE 44. SPECTRUM OF H_2-O_2 FLAME

narrow bandpass filters (sometimes referred to as spike filters) of known transmission characteristics. The bandwidth at the base is usually of the order of 0.1 to 0.2μ, and the wavelength for peak transmission is usually known to with $\pm$ 0.01 microns. The second method uses the well known molecular absorption bands of such vapors as H_2O, CO_2, Co, HCl. NH_3, etc.[7] Preliminary wavelength calibrations were obtained by utilizing both methods, since a small supply of filters was readily available. The absorption bands used were those of H_2O and CO_2 at the wavelengths 1.38, 1.87, 2.7, 3.2, and 4.3μ, as was mentioned earlier. In addition the absorption by a thin polystyrene film in the 3.3μ region was used. Figure 45 shows the spectrum in the 1 to 5μ region of a 1000°C blackbody source upon which the absorption from the aforementioned atmospheric bands and the polystyrene bands are shown. Although the polystyrene film contains many complex absorption bands, only the 3.3μ portion is within the scanning limits of the spectrometer.

Also shown in Figure 45 are some numerical figures which indicate the possible resolution of the instrument. Although these may not be the actual limits of resolution, the figures do show that a resolution capability of 0.1μ is by no means difficult to obtain. Since the primary function of the equipment is to scan rapidly over the wavelength regions of interest (1 to 5μ) because of short firing durations it is not expected that the actual resolution limits are too different from those shown. Also, since the objective of the present study is not to determine the fine structure of rocket flames but rather to determine the total radiation emitted, such a resolution capability is certainly adequate.

6.4 FUTURE WORK

With preparation of the optical system and instrumentation complete the final series of data runs for the contract will start. Additional radiancy calibrations will enable absolute radiancy levels to be determined on past as well as future runs. From these data, it should then be possible to determine spectral emissivities and cloud emissivities of various rocket flames.

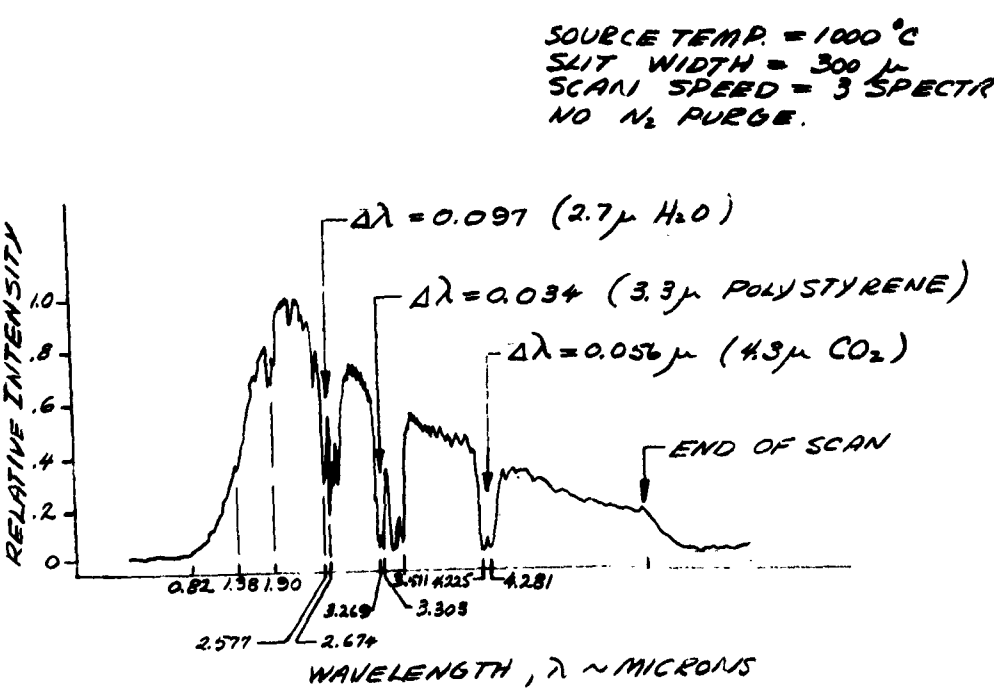

FIGURE 45. BLACKBODY SPECTRUM SHOWING ABSORPTION BY ATMOSPHERE AND BY A POLYSTYRENE FILM

REFERENCES

1. Price, F. C. et al., "Internal Environment of Solid Rocket Nozzles," Second Quarterly Technical Report, Aeronutronic Division of Philco Corporation, Publication No. U-2414, 19 December 1963.

2. Price, F. C. et al., "Internal Environment of Solid Rocket Nozzles," First Quarterly Technical Report, Aeronutronic Division of Philco Corporation, Publication No. C-2278, 30 September 1963.

3. Sehgal, R., "An Experimental Investigation of a Gas-Particle System," Jet Propulsion Laboratory, TR 32-238, 16 March 1962.

4. Jamieson, J. A., et al., Infrared Physics and Engineering, McGraw-Hill Book Company, Inc., New York, 1963.

5. Dobbins, R. A., "Measurement of Mean Particle Size in a Gas Particle Flow," AIAA Journal, Vol. 1, No. 8, 1940-1942, August 1963.

6. Jamieson, J. A., et al., Infrared Physics and Engineering, McGraw-Hill Book Company, Inc., New York, 1963.

7. Plyler, E. K., et al., "Vibration-Rotation Structure in Absorption Bands for the Calibration of Spectrometers from 2 to 16 Microns," Journal of Research of the National Bureau of Standards - A. Physics and Chemistry, Vol. 64, No. 1, January-February 1960.